

AD-A130 788

THE EFFECTS OF ATMOSPHERIC WATER VAPOR ABSORPTION ON
INFRARED LASER PROPAGATION (U) OHIO STATE UNIV COLUMBUS
ELECTROSCIENCE LAB L G WALTER MAY 83 ESL-713774-2

1/1

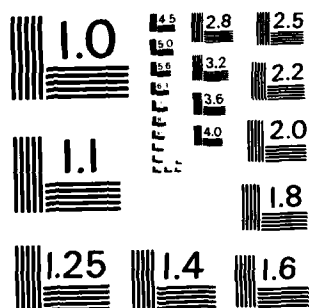
UNCLASSIFIED

ARO-17603.1-GS DAAG29-81-K-0084

F/G 20/14

NL

END
DATE
FILMED
*9 - 85
DTIC



MICROCOPY RESOLUTION TEST CHART
NATIONAL BUREAU OF STANDARDS - 1963 - A

OSU

The Ohio State University

THE EFFECTS OF ATMOSPHERIC WATER VAPOR ABSORPTION
ON INFRARED LASER PROPAGATION IN THE
5 MICROMETER BAND

L.G. Walter

The Ohio State University

ElectroScience Laboratory

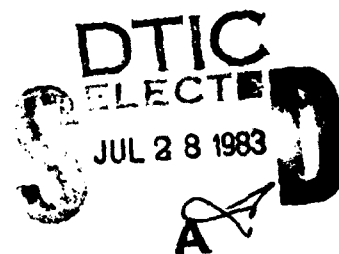
Department of Electrical Engineering
Columbus, Ohio 43212

Technical Report 713774-2

Contract DAAG29-81-K-0084

May 1983

Department of the Army
U.S. Army Research Office
P.O. Box 12211
Research Triangle Park, North Carolina 27709



This document has been approved
for public release and sale; its
distribution is unlimited.

83 07 27 00 4

DTIC FILE COPY

ADA130788

NOTICES

When Government drawings, specifications, or other data are used for any purpose other than in connection with a definitely related Government procurement operation, the United States Government thereby incurs no responsibility nor any obligation whatsoever, and the fact that the Government may have formulated, furnished, or in any way supplied the said drawings, specifications, or other data, is not to be regarded by implication or otherwise as in any manner licensing the holder or any other person or corporation, or conveying any rights or permission to manufacture, use, or sell any patented invention that may in any way be related thereto.

REPORT DOCUMENTATION PAGE		1. REPORT NO.	2.	3. Recipient's Accession No.
4. Title and Subtitle		5. Report Date		
THE EFFECTS OF ATMOSPHERIC WATER VAPOR ABSORPTION ON INFRARED LASER PROPAGATION IN THE 5 MICROMETER BAND		May 1983		
7. Author(s)		6.		
L. G. Walter		8. Performing Organization Rept. No.		
9. Performing Organization Name and Address		ESL-713774-2		
The Ohio State University ElectroScience Laboratory Department of Electrical Engineering Columbus, Ohio 43212		10. Project/Task/Work Unit No.		
12. Sponsoring Organization Name and Address		11. Contract(C) or Grant(G) No.		
Department of the Army, U.S. Army Research Office P.O. Box 12211 Research Triangle Park, North Carolina 27709		(C) (G) DAAG29-81-K-0084		
15. Supplementary Notes		13. Type of Report & Period Covered		
The work reported in this report was also used as a thesis submitted to The Ohio State University Department of Electrical Engineering as part of the requirements for the degree Master of Science.		Technical Report		
16. Abstract (Limit 200 words)		14.		
<p>The purpose of this study was to gather temperature dependent nitrogen broadened water vapor data at infrared frequencies of $1941.0952/\text{cm}^{-1}$, $1943.8624/\text{cm}^{-1}$, and $1949.2495/\text{cm}^{-1}$. This data is to be used to improve on the temperature characteristics of a far wing line shape model developed by M.E. Thomas and R.J. Nordstrom at The Ohio State University. In addition, the study investigated this $5.15 \mu\text{m}$ region for on-line/off-line resonance pairs for possible remote sensing of water vapor by DIAL techniques.</p> <p>The probe frequencies of $1941.0952/\text{cm}^{-1}$, $1943.8624/\text{cm}^{-1}$ and $1949.2495/\text{cm}^{-1}$ were generated by frequency doubling with a CdGeAs_2 crystal pumped by a CO_2 laser lasing on the R(12), R(14) and R(18) lines of the $[00^0_1 - 10^0_0]$ band, respectively.</p> <p>Due to experimental uncertainties in the data obtained during the study, only a general temperature characteristic of the absorption for the investigated laser lines was obtained. The data did show agreement with the far wing line shape model to a first order approximation; however, the study concluded that more accurate data is needed before a more detailed analysis can be made of the absorption versus temperature for these lines. A possible on-line/off-line pair for DIAL applications was also found - the doubled CO_2 R(18) and R(20) lines, respectively.</p>				
17. Document Analysis & Descriptors				
b. Identifiers/Open-Ended Terms				
c. COSATI Field/Group				
18. Availability Statement		19. Security Class (This Report)		21. No. of Pages
Approved for public release; distribution unlimited.		Unclassified		86
		20. Security Class (This Page)		22. Price
		Unclassified		

(See ANSI-Z39.18)

See Instructions on Reverse

TABLE OF CONTENTS

	Page
LIST OF TABLES	iv
LIST OF FIGURES	v
CHAPTER	
I. INTRODUCTION	1
II. THEORY	10
A. INTRODUCTION	10
B. THE LINE SHAPE	13
1. <u>Introduction</u>	13
2. <u>The Near Line Center Line Shape -</u> <u>Interuption Broadening</u>	19
3. <u>The Far Wing Line Shape - Statistical</u> <u>Broadening</u>	21
C. THE TOTAL LINE SHAPE, THE LINE STRENGTH AND THE ABSORPTION COEFFICIENT	24
III. EXPERIMENTAL APPARATUS, TESTS, AND PROCEDURES	28
A. INTRODUCTION	28
B. THE EXPERIMENTAL APPARATUS	28
1. <u>The CO₂ Laser</u>	28
2. <u>Second Harmonic Generation</u>	33
3. <u>The External Optical System</u>	39
4. <u>The 10.785 Meter Multipass Absorption Cell</u>	39
5. <u>The Computer Controlled Data Acquisition System</u>	43

	Page
C. TESTS	46
1. <u>DC Amplifier and A/D Calibration</u>	46
2. <u>The Lock-in Amplifiers</u>	48
D. EXPERIMENTAL PROCEDURES	48
1. <u>Introduction</u>	48
2. <u>Optical Alignment</u>	48
3. <u>Background Measurements</u>	49
4. <u>Sample Handling</u>	51
5. <u>Transmittance Measurements</u>	52
IV. DATA ANALYSIS	54
A. INTRODUCTION	54
B. SELECTION OF THE INVESTIGATED FREQUENCIES, TEMPERATURES AND PRESSURES	54
C. DATA PRESENTATION AND ANALYSIS	60
1. <u>Data Presentation</u>	60
2. <u>The Empirical Expression for the Absorption Coefficient</u>	73
3. <u>A Least Squared Curve Fit to the Data and Analysis</u>	76
V. CONCLUSIONS	79
REFERENCES	84

A



LIST OF TABLES

TABLE		Page
2.1	CHARACTERISTICS OF MOLECULAR COLLISIONS	16
3.1	TYPICAL OUTPUT POWER FOR EACH CO ₂ LASER LINE	29
3.2	H ₂ O SAMPLE VOLUMES REQUIRED TO ESTABLISH PARTIAL PRESSURE OF 5, 10, AND 15 TORR AT TEMPERATURES OF 295°K, 310°K AND 323°K.	52
4.1	EXPERIMENTAL CONDITIONS FOR THE PURE H ₂ O SPECTRA SHOWN IN FIGURES 4.1a AND 4.1b (PATH LENGTH = 821 METERS).	56
4.2	NITROGEN BROADENED H ₂ O ABSORPTION DATA GATHERED FOR THE 2ν[R(12)] = 1941.096 cm ⁻¹ CO ₂ LASER LINE.	61
4.3	NITROGEN BROADENED H ₂ O ABSORPTION DATA GATHERED FOR THE 2ν[R(14)] = 1943.862 cm ⁻¹ CO ₂ LASER LINE.	62
4.4	NITROGEN BROADENED H ₂ O ABSORPTION DATA GATHERED FOR THE 2ν[R(18)] = 1949.245 cm ⁻¹ CO ₂ LASER LINE.	63
4.5	EXPERIMENTAL AND THEORETICAL ABSORPTION COEFFICIENT $k(\text{km}^{-1}) = A_p + B_p^2$ WITH WATER PRESSURE p IN TORR FOR THE INVESTIGATED LASER LINES.	77

LIST OF FIGURES

FIGURE	Page
1.1 Low resolution solar spectrum compared with laboratory spectra of atmospheric gasses [9].	3
1.2 Comparison of experimental and theoretical pressure dependence of water vapor continuum absorption at 944.1945 cm^{-1} .	5
1.3 Comparison of experimental and theoretical pressure dependence of water vapor continuum absorption at 944.1945 cm^{-1} .	7
2.1 Radiation transmission in a lossy medium.	11
2.2 The line shape function.	14
2.3 The correspondence between impact parameter and the line shape region.	17
2.4 The correlation function.	18
2.5 $p(\nu)$ versus $\Delta\nu$.	25
3.1 Schematic diagram of the laser optics and plasma tube.	31
3.2 CdGeAs ₂ crystal liquid nitrogen dewar.	34
3.3 1.5 meter CO ₂ laser.	34
3.4 Polarization of input and output fields for second harmonic Type-I phase matching.	35
3.5 Illustration of the elliptical characteristics of the index of refraction as a function of the spatial orientation of polarization for an electro-magnetic wave propagating through a typical nonlinear crystal.	37
3.6 Optical system external to the absorption cell.	40
3.7 Example of spot pattern on field mirror for a path length of 217.2 meters.	42

FIGURE	Page
3.8 Block diagram of data acquisition system.	44
3.9 Calibration data for the signal and reference channels. The error in mV is plotted versus theoretical output.	47
4.1a. Location of laser lines $2\nu[R(12)]$, $2\nu[R(14)]$, $2\nu[R(16)]$ and $2\nu[R(18)]$ in the spectral region under investigation.	57
4.1b. Location of the laser line $2\nu[R(20)]$ in the spectral region under investigation.	58
4.2 Comparison of experimental and theoretical H_2O partial pressure dependence for $2\nu[R(12)] = 1941.0958 \text{ cm}^{-1}$ at 295 K° .	64
4.3 Comparison of experimental and theoretical H_2O partial pressure dependence for $2\nu[R(12)] = 1941.0958 \text{ cm}^{-1}$ at 310 K° .	65
4.4 Comparison of experimental and theoretical H_2O partial pressure dependence for $2\nu[R(12)] = 1941.0958 \text{ cm}^{-1}$ at 323 K° .	66
4.5 Comparison of experimental and theoretical H_2O partial pressure dependence for $2\nu[R(14)] = 1943.8618 \text{ cm}^{-1}$ at 295 K° .	67
4.6 Comparison of experimental and theoretical H_2O partial pressure dependence for $2\nu[R(14)] = 1943.8618 \text{ cm}^{-1}$ at 310 K° .	68
4.7 Comparison of experimental and theoretical H_2O partial pressure dependence for $2\nu[R(14)] = 1943.8618 \text{ cm}^{-1}$ at 323 K° .	69
4.8 Comparison of experimental and theoretical H_2O partial pressure dependence for $2\nu[R(18)] = 1949.2452 \text{ cm}^{-1}$ at 295 K° .	70
4.9 Comparison of experimental and theoretical H_2O partial pressure dependence for $2\nu[R(18)] = 1949.2452 \text{ cm}^{-1}$ at 310 K° .	71
4.10 Comparison of experimental and theoretical H_2O partial pressure dependence for $2\nu[R(18)] = 1949.2452 \text{ cm}^{-1}$ at 323 K° .	72

CHAPTER I

INTRODUCTION

The transmission of infrared radiation through the atmosphere is of considerable interest to many disciplines of science and a drive to better understand the various attenuation processes of molecular absorption and aerosol scattering constantly goes on. These attenuation processes are particularly dependent on tropospheric concentrations of H_2O and CO_2 as well as aerosol concentrations. Water vapor absorption dominates much of the infrared spectrum and affects the performance of many E-O systems. This absorption is directly dependent on the concentration of water vapor molecules along the atmospheric path of interest.

Some of these E-O systems include laser radar or LIDAR systems which can measure atmospheric water vapor profiles, temperature profiles and gaseous pollutant concentrations. Other infrared systems include optical data transmission links, laser range finders, and infrared laser target designators. Some passive infrared systems include thermal imagers and Forward-Looking Infrared (FLIR).

These systems are largely confined to the optical windows or regions where the attenuation is small. Figure 1.1 shows that the infrared windows of the troposphere occur between 13 to 8 μm , 5 to 4.5 μm and 4.1 to 3.2 μm , and are bounded by strong H_2O and CO_2 absorption regions. The weak absorption of the window regions is caused by local line and continuum absorption.

Continuum absorption is a depression of the spectral background throughout the infrared spectrum which appears as a slowly varying function of frequency. While many continuum studies have been done in the 10 μm region [1,2,3,4,5], not nearly as much has been done in the 3 to 5 μm band [6,7]. This is mostly because the continuum absorption in this region is an order of magnitude smaller than the continuum absorption in the 8 to 13 μm region. Although there is greater continuum interest in the 8 to 13 μm band, more data is needed from the 3 to 5 μm band to gain a clearer picture of the entire continuum effect.

In 1938, based on his observations of the 8 to 12 μm band, W.M. Elsasser [8] suggested the existence of a water vapor continuum and speculated that it was caused by the far wings of very strong water vapor lines outside the window region. However, a line by line computation of the continuum absorption by Burch [2], using a Lorentzian line shape, yielded absorption coefficients less than actually observed for the 10 μm band. In addition, the absorption from wings of these Lorentzian line shapes in the 10 μm band increases with increasing temperature, whereas experiment has shown that the actual continuum

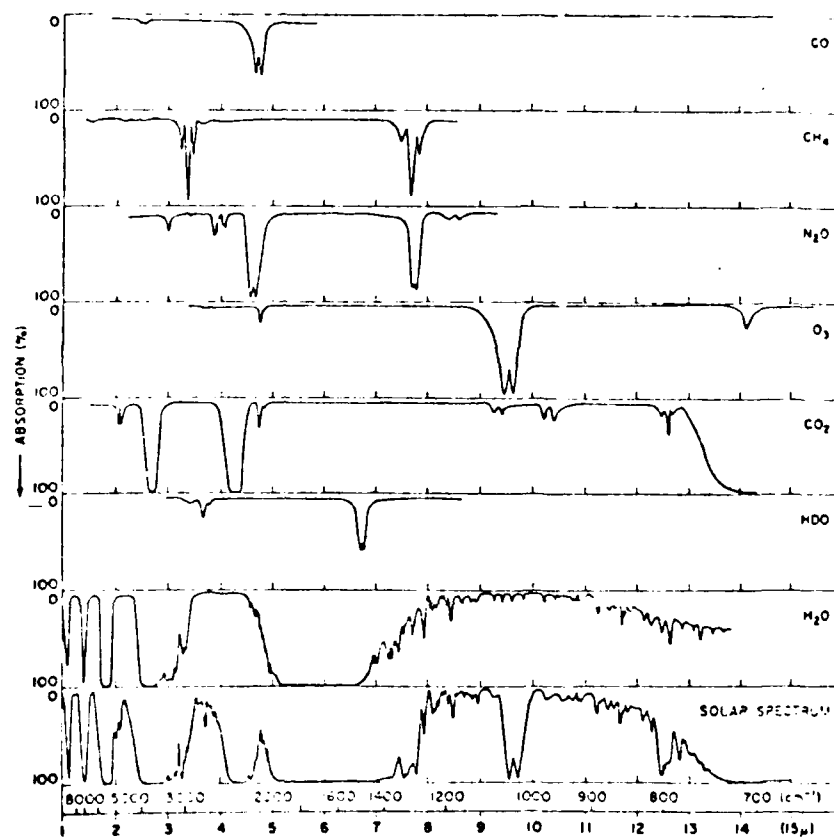


Figure 1.1 Low resolution solar spectrum compared with laboratory spectra of atmospheric gasses [9].

absorption has a negative temperature dependence, that is, it decreases with increasing temperature [9].

This failure of the Lorentzian far wings to model the continuum has popularized a theory of continuum absorption which bases the phenomenon on water dimers [10,11] or larger, more complex clusters or aggregates [12,13] creating intense, unresolved absorption bands throughout the infrared spectrum. The theory argues that, though the number of these complex aggregates is small, their effect could easily be seen in the window regions. Most importantly, the dimer theory does explain the negative temperature dependence of the continuum for it is argued that the attenuation is proportional to the number of aggregates which, in turn, is proportional to $\exp(-\Delta H/kT)$, where ΔH is the change in enthalpy on aggregate formulation and is negative. Thus, the attenuation will show a negative dependence on temperature.

The inability of the Lorentz line shape to correctly predict the magnitude, temperature, and pressure dependence of the water vapor continuum has made the dimer theory popular. In 1979, however, M.E. Thomas and R.J. Nordstrom at The Ohio State University [14] developed a line shape which is Lorentzian out to 5 cm^{-1} from line center but is modified beyond 5 cm^{-1} . Figure 1.2 shows the inability of the Lorentz line shape to model the water vapor pressure dependence of the nitrogen broadened absorption coefficient at room temperature for the P(24) CO_2 laser line (940.548 cm^{-1}). If only the absorption lines within the commonly used $\pm 20 \text{ cm}^{-1}$ bound are involved in the calculation, the

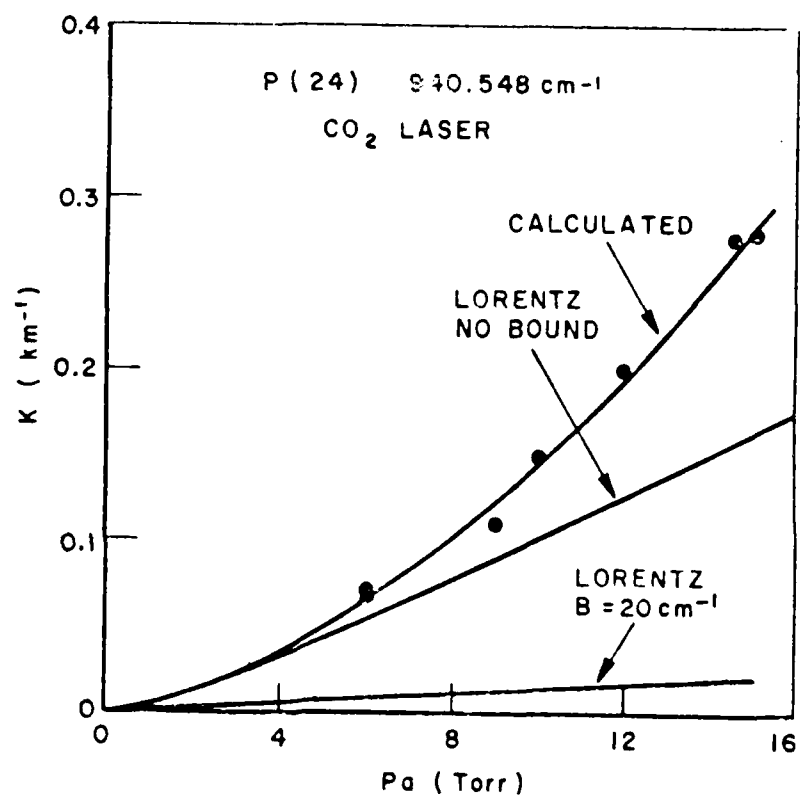


Figure 1.2 Comparison of experimental and theoretical pressure dependence of water vapor continuum absorption at 944.1945 cm⁻¹.

Lorentz shape falls far below the actual data plot. But when the bound is extended to all absorption lines between 0 and 2300 cm^{-1} , the Lorentz line shape does a much better job of modeling the data. Both of the above calculations used the AFGL line listing [15]. Now observe how well the Thomas-Nordstrom non-Lorentzian line shape (or TN model) models the pressure dependence of the absorption continuum for this $10\text{ }\mu\text{m}$ window line.

Their study demonstrated the importance of far wing phenomena in modeling water vapor continuum absorption by first quantum mechanically deriving a model for water vapor nitrogen interactions, and then fitting the model to data from regions dominated by strong local line absorption by fine tuning their line shape parameters. After the line shape parameters had been determined in this region, they successfully applied the model to the window regions where continuum absorption dominates. Data from grating spectrometer measurements from 300 cm^{-1} to 650 cm^{-1} [16], and HF [17] and CO [18] laser measurements in the $3\text{ }\mu\text{m}$ and $5\text{ }\mu\text{m}$ spectral regions respectively, was used to obtain the far wing line shape parameters needed for the TN model. They referred to these parameters as the "A" and "G" parameters.

After the "A" and "G" parameters were determined by curve fit to the above mentioned data, the line shape model was applied to the 4 and $10\text{ }\mu\text{m}$ window regions with great success particularly in modeling the pressure dependence of the continuum absorption coefficient. A negative temperature dependence was predicted by this model but not quite at the rate actually observed, as Figure 1.3 illustrates. This lack of

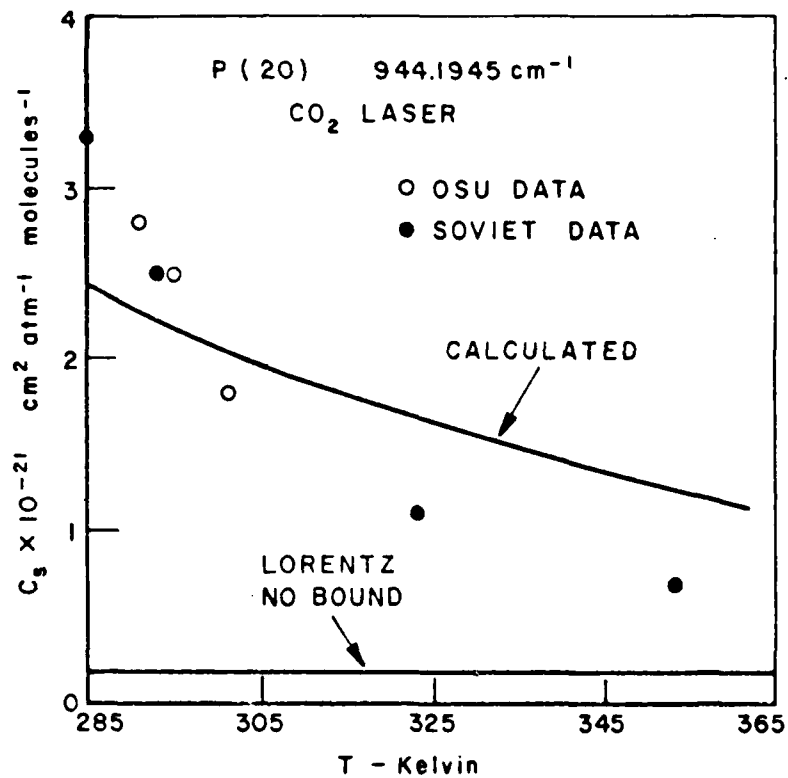


Figure 1.3 Comparison of experimental and theoretical pressure dependence of water vapor continuum absorption at 944.1945 cm⁻¹.

agreement is attributed to the inaccuracies of the interaction potentials and the perturbation expansions of the molecular collision Hamiltonian.

In addition, accurate temperature dependence data does not exist for any of the absorption bands of H_2O in the infrared spectral region. With the aid of such data, significant improvements and refinements in the line shape parameters could be made and thus improve the model's ability to predict the negative temperature dependence of the continuum.

It is the primary objective of this study to gather temperature dependence data in the $5\text{ }\mu\text{m}$ spectral region, which is close to the $6.3\text{ }\mu\text{m}$ ν_2 band center and dominated by strong local line absorption, in order to lay the foundation for future studies aimed at improving the line shape parameters developed by Thomas and Nordstrom. Specifically, this data should aid in improving the temperature dependence of these far wing parameters.

If these far wing parameters are to be used in truly modeling continuum absorption, they must be independent of the continuum. For this reason, data must be taken in regions where local line absorption dominates. Absorption coefficients on the order of 1 to 30 km^{-1} have been obtained in the $5.3\text{ }\mu\text{m}$ region where the continuum contribution is only about 0.1 km^{-1} , from 1 to 2 orders of magnitude smaller than the local line absorbance.

Data was obtained through the use of a multiple pass absorption cell and a frequency doubled, line selectable cw CO_2 laser. The

second harmonic generation was achieved outside the laser cavity by a high efficiency CdGeAs₂ crystal. The doubled CO₂ laser exhibits a spectral range from 4.6 to 5.3 μm which is similar to a nitrogen cooled CO laser's spectral range. The doubled CO₂ laser system was selected over the CO laser because it is much easier and less expensive to operate and more importantly, allowed the opportunity to collect data at frequencies different from previous CO laser studies, thus enhancing the picture of the spectral line shapes in this high absorption region.

This thesis is primarily intended as a progress report and to aid in future attempts to gather more accurate data using the frequency doubled CO₂ laser probe system. The data which will be presented in Chapter IV needs to be further refined and verified by more data acquisition. This thesis offers recommendations as to how more accurate data can be obtained in the future.

Chapter II will qualitatively develop the general expression for the absorption coefficient given by the Thomas-Nordstrom model [14] which was originally developed here at The Ohio State University in 1976-79. Then, Chapter III will discuss the experimental apparatus, calibration tests, and procedures used to acquire the data which will be presented and analyzed in Chapter IV. Both Chapters III and IV will point out the various problems encountered with experiment and data analysis and Chapter V will offer a summary of the project goals and conclude with recommendations for future data acquisition.

CHAPTER II

THEORY

A. INTRODUCTION

The general expression for the absorption coefficient developed in detail by Michael E. Thomas and Robert J. Nordstrom at The Ohio State University [14] is qualitatively developed in this chapter. Section B develops the near line center and far wing line shapes separately and Section C presents the total line shape, the line strength and the final general expression for the absorption coefficient for $\text{H}_2\text{O}-\text{N}_2$ gaseous mixtures.

Consider Figure 2.1 which illustrates the propagation and attenuation of monochromatic radiation by an absorbing medium. The change in intensity dI per unit length $d\ell$ can be written as

$$\frac{dI}{d\ell} = -\sigma I \quad (1)$$

where σ is the extinction coefficient which can further be broken down into two mechanisms:

$$\sigma = k + s \quad (2)$$

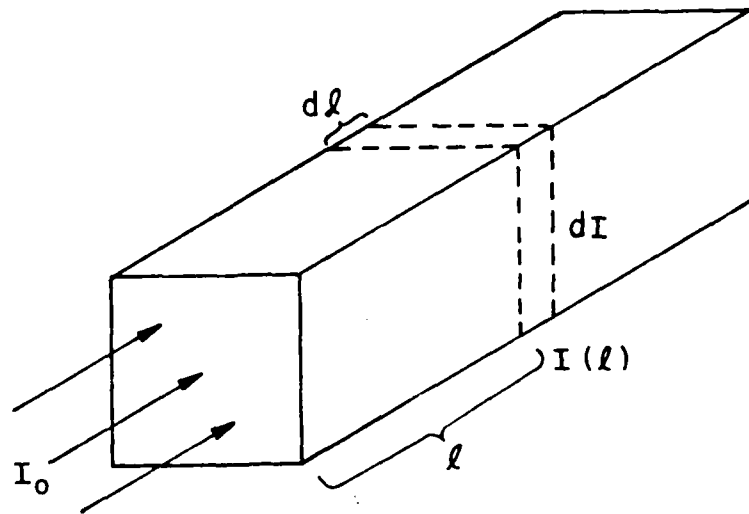


Figure 2.1 Radiation transmission in a lossy medium.

where k is the absorption coefficient and s is the scattering coefficient.

This study is restricted to infrared propagation through a gaseous medium ($a \ll \lambda$) thus making the scattering effects of little significance. In addition, scattering is at least a two photon process where absorption is a single photon process. In the perturbation expansion of the photon and absorber interaction Hamiltonian, the single photon process will dominate. So the absorption mechanism is the dominant term in the extinction coefficient and Equation (2) can be simplified to just the absorption term,

$$\sigma = k \quad . \quad (3)$$

The absorption coefficient indicates the probability of a molecular interaction with an electromagnetic field and other molecular systems resulting in the absorption of a photon and the excitation of the absorbing molecule.

Lambert's law is arrived at by the substitution of Equation (3) into Equation (1)

$$\frac{dI}{d\ell} = -kI \quad . \quad (4)$$

The solution of this simple differential equation yields the transmittance through the absorbing medium as Equation (5) shows,

$$T = e^{-k\ell} \quad (5)$$

where

$$T = \frac{I(\ell)}{I(0)} \quad .$$

The absorption coefficient $k(\nu)$ can be expressed as a sum of the attenuation effects of n absorption lines,

$$k(\nu) = \sum_{i=1}^n S_i j_i (\nu - \nu_0; \alpha) \quad (6)$$

where S_i is the line strength of the i^{th} absorption line, and $j_i(\nu-\nu_0; \alpha)$ is the line shape function of the i^{th} absorption line centered at frequency ν_0 and α is the half width at half maximum of the i^{th} line.

The line shape function is normalized by the requirement that

$$\int_0^{\infty} j(\nu-\nu_0; \alpha) d\nu = 1 \quad (7)$$

for all i from 1 to n . Thus, the absorption coefficient can be divided into a line strength factor and a line shape factor.

B. THE LINE SHAPE

1. Introduction

The two general classifications of line shapes are homogeneous and inhomogeneous broadened line shape. Homogeneous broadening means that the line shapes have the same basic shape for each molecule and that the shape observed for a number of molecules will be the same as the shape observed for one molecule. Natural broadening and collision broadening are examples of homogeneous broadening. Inhomogeneously broadened lines are a collection of frequency shifted homogeneously broadened lines and the line shape for a single molecule may be completely different than the shape seen for a collection of molecules. One example of inhomogeneous broadening is Doppler broadening.

Homogeneous broadening will dominate for the pressure and temperature range for which this model is valid and thus will be the only type of broadening considered in this line shape development.

The homogeneous line shape can be broken up into three regions: the near line center region, intermediate region, and far wing region as shown in Figure 2.2 and Equation (8),

$$j_c(\omega) = j_{CFW}(\omega) + j_{CIW}(\omega) + j_{CNLC}(\omega) \quad (8)$$

The general form of each shape is

$$j_c(\omega) = \frac{Re}{\pi} \int_0^{\infty} d\tau \exp(-i\Delta\omega\tau) C(\tau) \quad (9)$$

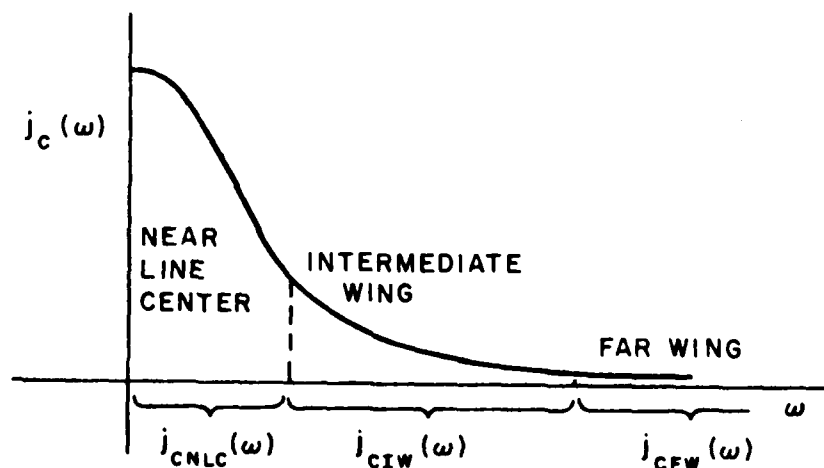


Figure 2.2 The line shape function.

where $C(\tau)$ is the time correlation function for two energy transition levels of the absorbing molecule perturbed by another molecule through a collision. The lines labeled 1 and 2 in Figure 2.3 represent two possible collision paths the broadening molecule might have in relation to the absorbing molecule.

Table 2.1 lists the characteristics of the collision in each region. The strong collisions typical of collision path 1 greatly shift the energy level of the absorbing molecule and thus are responsible for the far wing line shape; whereas the weak collisions typical of collision path 2 only slightly perturb the absorber molecular energy level and therefore the energy shift from line center is very small as compared to the far wing shift.

The general correlation function $C(\tau)$ is shown in Figure 2.4. It can be shown that this function is symmetric about $\tau = 0$ which allows the change in integration limits for Equation (9) resulting in the form shown in Equation (10),

$$\begin{aligned}
 j_c(\omega) &= \frac{1}{2\pi} \operatorname{Re} \int_{-\infty}^{\infty} d\tau \exp(-i\Delta\omega\tau) \exp(i\omega_0\tau) C(\tau) \\
 &= \operatorname{Re} F^{-1} \{ \exp(i\omega_0\tau) C(\tau) \}
 \end{aligned}
 \tag{10}$$

Thus, the line shape function $j_c(\omega)$ and the function $\exp(i\omega_0\tau)C(\tau)$ are

TABLE 2.1

CHARACTERISTICS OF
MOLECULAR COLLISIONS

$R > R_a$	Very little effect on absorbing molecule
$R_a > R > R_b$	Interruption broadening [46] - near line center phenomena <ol style="list-style-type: none"> 1. Brief duration of collision 2. Time between collisions is long compared to duration of collisions 3. Binary collisions 4. Long correlation time
$R_b > R > R_c$	Intermediate region - difficult to model <ol style="list-style-type: none"> 1. Many body problem
$R_c > R$	Statistical broadening [46] - far wing <ol style="list-style-type: none"> 1. Binary collisions 2. Duration of collision $\sim \frac{2R}{v}$ 3. Short correlation time

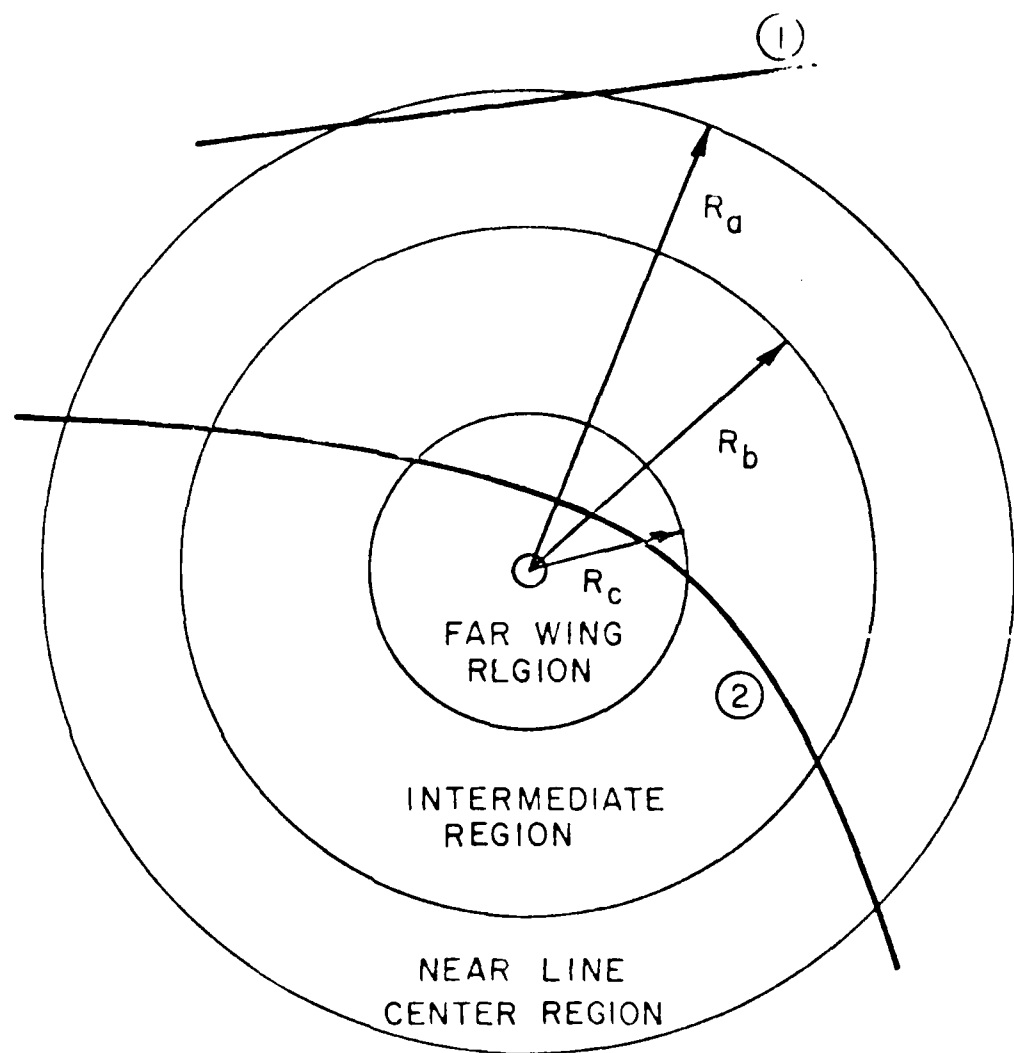


Figure 2.3 The correspondence between impact parameter and the line shape region.

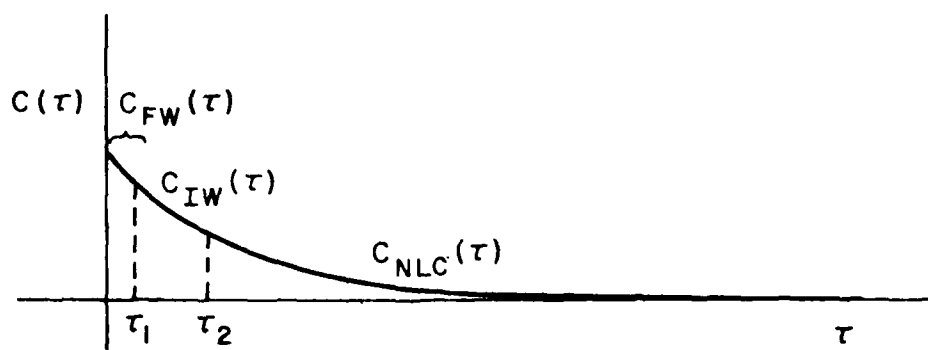


Figure 2.4 The correlation function.

related by the Fourier transform. The time-bandwidth product of the Fourier transform theory,

$$\Delta\tau\Delta\omega = 1 \quad (11)$$

further demonstrates how the strong collisions, with short correlation times $\Delta\tau$ must result in large frequency deviations from line center $\Delta\omega$ in order to satisfy Equation (11).

The functional form of the line shape is arrived at by substituting Equation (10) into Equation (9), thus resulting in Equation (12),

$$\begin{aligned} j_c(\omega) &= j_{cFW}(\omega) + j_{cIW}(\omega) + j_{cNLC}(\omega) \\ &= \text{Re } F^{-1} \{e^{j\omega_0\tau} C_{FW}(\tau)\} + \text{Re } F^{-1} \{e^{j\omega_0\tau} C_{IW}(\tau)\} \\ &\quad + \text{Re } F^{-1} \{e^{j\omega_0\tau} C_{NLC}(\tau)\} \end{aligned} \quad (12)$$

The near line center and far wing line shapes can be determined with a great deal of work but the intermediate region line shape is nearly impossible to determine. This region will be determined by a mixing of the near line center and the far wing line shape functions in Section 3.

2. The Near Line Center Line Shape - Interruption Broadening

The conditions for the near line center phenomena of interruption broadening or impact broadening are listed in Table 2.1. Because the interaction time is brief under these conditions, the correlation function can be examined between $C(\tau)$ and $C(\tau+d\tau)$ where $d\tau \ll \tau$. That is, the same correlation function applies at τ and $\tau+d\tau$. The result is that the correlation function appears as a monotonic decay during this time interval which can be expressed as a simple exponential of the form

$$C(\tau) = \exp(-\alpha\tau) \quad . \quad (13)$$

From Equation (13), the line shape becomes

$$j_{\text{CNLC}}(\omega) = \frac{1}{\pi} \frac{\alpha}{\Delta\omega^2 + \alpha^2} \quad (14)$$

which is the Lorentz line shape and α the halfwidth.

The temperature dependence of α is difficult to derive. A second order perturbation expansion of the molecular interaction potentials yields a temperature dependence of the form

$$\alpha \propto \frac{1}{\sqrt{T}} \quad . \quad (15)$$

However, the form is not always observed [19,20]. Using another method which looks at the molecular perturbations strictly as phase modulations of the eigenstates, called the phase shift or phase modulation method, leads to a temperature dependence of the form

$$\alpha \propto \frac{1}{T} \quad (16)$$

for the dipole-dipole interactions found in self-broadening and

$$\alpha \propto \frac{1}{T^{0.83}} \quad (17)$$

for dipole-quadrupole interactions found in foreign-broadening. The form showing the pressure and temperature dependence of the halfwidth is shown in Equation (18)

$$\alpha = \alpha_0 \left(\frac{296}{T} \right)^{.83} \left[B \left(\frac{296}{T} \right)^{.17} p_a + p_b \right] \quad (18)$$

where

$$\alpha_0 \left(\frac{296}{T} \right)^{.83} p_b = \alpha_{\text{FOREIGN BROADENED}}$$

$$B = \frac{\alpha_{\text{SELF BROADENED}}}{\alpha_{\text{FOREIGN BROADENED}}}$$

p_a = absorber pressure

p_b = broadener pressure

T = temperature

3. The Far Wing Line Shape - Statistical Broadening

The far wing phenomena, or statistical broadening, is characterized by short correlation functions resulting from strong binary molecular interactions. Due to the strength of such interactions, no perturbation theory can be applied. However, the phase shift method briefly described in the last section can be used for statistical broadening to determine the far wing line shape. That is, by considering the phase shift effects in the eigenstates to all orders, brought about by the strong molecular interactions during photon absorption, the far wing line shape can be approximated.

This phase shift or phase modulation theory and another statistical theory used by Fomin and Tvorogov [21] yield the same leading term for the far wing shape

$$j_{\text{CFW}}(\omega) \propto \frac{1}{(\Delta\omega)^{1+3/m_j}} \quad (19)$$

where $m_j = 6$ for self-broadening and $m_j = 4$ for foreign-broadening by N_2 or O_2 . A more exact expression for the far wing shape resulting from the phase shift method is shown in Equation (20),

$$j_{\text{CFW}}(\nu) = \frac{1}{\pi} \left[\frac{.6266 \lambda_{a6}}{|\nu - \nu_0|^{1.5}} + \frac{.8491 \lambda_{b4}}{|\nu - \nu_0|^{1.75}} \right] \quad (20)$$

where

ν_0 = wavenumber at line center

$$\lambda_{a6} = A1(\nu) \left(\frac{296}{T} \right)^{1.5} p_a$$

$$\lambda_{b4} = A2(\nu, J) \left(\frac{296}{T} \right)^{1.5} p_b$$

ν = vibrational quantum number

J = rotational quantum number.

The frequency ω (radians/second) has been replaced by the wavenumber ν (cm^{-1}). λ_{a6} and λ_{b4} are very complicated functions of the interaction potentials between $\text{H}_2\text{O} - \text{H}_2\text{O}$ and $\text{H}_2\text{O} - \text{N}_2$ interactions, respectively.

$A1(\nu)$ will be different for every vibrational quantum number of the absorber but is independent of the rotational quantum number due to the $\text{H}_2\text{O} - \text{H}_2\text{O}$ interaction characteristics. However, $A2(\nu, J)$ does depend on both the vibrational and rotational quantum numbers. Since the potential function for the near line center and far wing phenomena are the same, the j -dependence of $A2(\nu, J)$ can be written as

$$A2(\nu, J) = A2(\nu)(19.919) \left(\frac{\alpha_0}{0.07} \right)^{1.125} \quad (21)$$

where 0.07 represents a mean value for α_0 . $A1(\nu)$ and $A2(\nu)$ are two of the four parameters in the TN model that were determined experimentally because of the complex nature of the terms that make up the parameters and the uncertainty of the interaction potentials. As stated in Chapter I, it is the intent of this study to gather data that can be used to

improve upon the temperature modeling capability of the TN "A" parameters just described and the TN "G" parameters which will be described shortly.

Equation (22) shows the form that the far wing shape takes on after it is normalized to one (i.e., $\int_0^{\infty} j_{cVW}(\nu) d\nu = 1$),

$$J_{cFW}(\nu) = \frac{1}{\pi} \left[\frac{.3198\lambda_{a6}}{|\Delta\nu|^{1.5+(\lambda_{a6})^3}} + \frac{.4334\lambda_{b4}}{|\Delta\nu|^{1.75+(\lambda_{b4})^{7/3}}} \right] . \quad (22)$$

There is one final correction that must be made in the far wing line shape. The phase shift method used to develop Equation (22) requires an energy level shift or frequency modulation correction factor which was determined by Fomin and Tvorogov [21]. When this level shift correction is applied to the far wing shape, Equation (22) becomes

$$j_{cFW}(\nu) = \frac{1}{\pi} \left[\frac{.3198\lambda_{a6}}{|\Delta\nu|^{1.5+(\lambda_{a6})^3}} \exp(-G_{a6}(\nu)\sqrt{\Delta\nu}) \right. \\ \left. + \frac{.4334\lambda_{b4}}{|\Delta\nu|^{1.75+(\lambda_{b4})^{7/3}}} \exp(-G_{b4}(\nu)\sqrt{\Delta\nu}) \right] \quad (23)$$

where the "G" parameters are functions of the vibrational quantum number of the absorber. The temperature dependence of the "G" parameters is of the form shown in Equations (24) and (25),

$$G_{a6}(\nu) = G_a(\nu) \left(\frac{296}{T} \right)^{.67} \quad (24)$$

$$G_{b4}(\nu) = G_b(\nu) \left(\frac{295}{T} \right)^{.67} . \quad (25)$$

These are the remaining two of the total four parameters which had to be experimentally determined for the TN model.

C. THE TOTAL LINE SHAPE, THE LINE STRENGTH AND THE ABSORPTION COEFFICIENT

The only remaining portion of the line shape to be determined is in the intermediate region. By choosing band pass and band stop filters centered at ν_0 , with slow fall off, a mixing of the interruption and statistical line shapes, respectively, can be achieved in this region. Thus the total line shape will have the form

$$j_c(\nu) = N(j_{cNLC}(\nu)p(\nu) + j_{cFW}(\nu)(1-p(\nu))) \quad (26)$$

where N is the normalization constant determined by evaluating Equation (27),

$$\int_0^{\infty} d\nu j_c(\nu) = 1 . \quad (27)$$

The pass filter function was chosen to be of the form shown in Equation (28) and displayed in Figure 2.5,

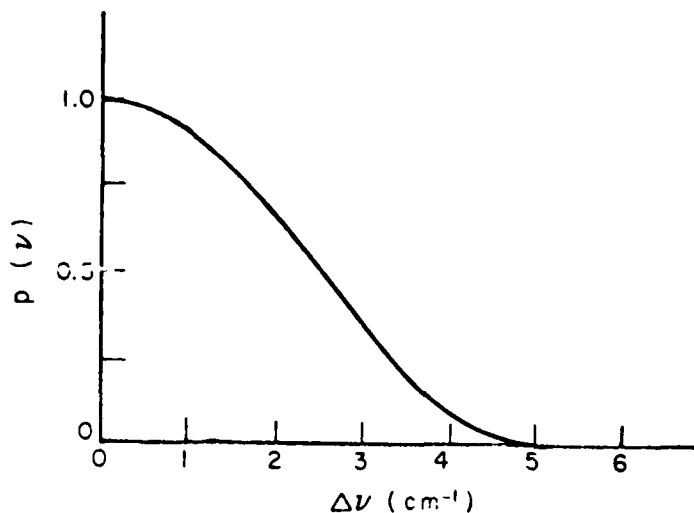


Figure 2.5 $p(v)$ versus Δv .

$$p(v) = \begin{cases} \frac{1}{2} + \frac{1}{2} \cos \frac{\pi \Delta v}{5} & |\Delta v| < 5 \text{ cm}^{-1} \\ 0 & |\Delta v| > 5 \text{ cm}^{-1} \end{cases} \quad (28)$$

This allows the interruption broadening line shape to dominate near line center and the band stop filter $(1-p(v))$ allows the statistical broadening line shape to dominate in the far wings beyond 5 cm^{-1} (50 to 100 halfwidths from line center).

One additional term shown below must multiply the line shape function for $\nu_0 < 1000 \text{ cm}^{-1}$,

$$\frac{\nu}{\nu_0} \frac{(1 - e^{-\nu h c / k T})}{(1 - e^{-\nu_0 h c / k T})} .$$

This term accounts for the Maxwell-Boltzman population statistics away from line center and this term is essentially equal to one for $\nu_0 > 1000 \text{ cm}^{-1}$. Therefore, it is not included for that range in order to improve the absorption coefficient computation time.

The line strength is derived by considering the transition rates from both the lower to upper states and the upper to lower states and can be shown to have the following form,

$$S_{lu} = S_{lu}^0 \frac{T_0 p_a}{T p_{a_0}} \left(\frac{T_0}{T}\right)^{1.5} e^{\frac{E_l(T-T_0)}{kT_0}} \frac{(1 - e^{-\nu_0 hc/kT})}{(1 - e^{-\nu_0 hc/kT_0})} \quad (29)$$

where

S_{lu}^0 = the line strength at standard pressure and temperature

$T_0 = 296^\circ\text{K}$

$p_{a_0} = 1 \text{ atm}$.

The total absorption coefficient for $\text{H}_2\text{O} - \text{N}_2$ mixtures is given in Equation (30),

$$k(\nu) = \sum_i k_i(\nu) = \sum_{lu} S_{lu}(\nu) j_c(\nu) \quad (30)$$

The summation is over all water vapor transitions. Using the form shown in Equation (26), the $\text{H}_2\text{O} - \text{N}_2$ absorption coefficient becomes

$$k(\nu) = \sum_{\ell u} S_{\ell u} N [j_{\text{CNLC}}(\nu) p(\nu) + j_{\text{CFW}}(\nu) (1-p(\nu))] \quad (31)$$

where

$$S_{\ell u} = S_{\ell u}^0 \frac{T_0 p_a}{T p_{a_0}} \left(\frac{T_0}{T}\right)^{1.5} e^{\frac{E_{\ell u}(T-T_0)}{kT_0}} \frac{(1-e^{-\nu_0 hc/kT})}{(1-e^{-\nu_0 hc/kT_0})}$$

$$j_{\text{CNCL}}(\nu) = \begin{cases} \frac{1}{\pi} \frac{\nu}{\nu_0} \frac{(1-e^{-\nu hc/kT})}{(1-e^{-\nu_0 hc/kT})} \frac{\alpha r}{((\Delta\nu)^2 + (\alpha r)^2)} & \nu_0 < 1000 \text{ cm}^{-1} \\ \frac{1}{\pi} \frac{\alpha r}{(\Delta\nu)^2 + (\alpha r)^2} & \nu_0 > 1000 \text{ cm}^{-1} \end{cases}$$

$$j_{\text{CFW}}(\nu) = \begin{cases} \frac{1}{\pi} \frac{(1-e^{-\nu hc/kT})}{(1-e^{-\nu_0 hc/kT})} \left[\frac{.3198 \lambda_{a6} e^{-G_{a6} \sqrt{\Delta\nu}}}{|\Delta\nu|^{1.5+\lambda_{a6}^3}} \frac{.4334 \lambda_{b4} e^{-G_{b4} \sqrt{\Delta\nu}}}{|\Delta\nu|^{1.75+\lambda_{b4}^{7/3}}} \right] & \nu_0 < 1000 \text{ cm}^{-1} \\ \frac{1}{\pi} \left[\frac{.3198 \lambda_{a6} e^{-G_{a6} \sqrt{\Delta\nu}}}{|\Delta\nu|^{1.5+\lambda_{a6}^3}} \frac{.4334 \lambda_{b4} e^{-G_{b4} \sqrt{\Delta\nu}}}{|\Delta\nu|^{1.75+\lambda_{b4}^{7/3}}} \right] & \nu_0 > 1000 \text{ cm}^{-1} \end{cases}$$

The normalization constant, N, is determined by

$$N^{-1} = \int_0^{\infty} j_{\text{CNLC}}(\nu) p(\nu) d\nu + \int_0^{\infty} j_{\text{CFW}}(\nu) (1-p(\nu)) d\nu \quad (32)$$

CHAPTER III

EXPERIMENTAL APPARATUS, TESTS AND PROCEDURES

A. INTRODUCTION

This chapter describes the apparatus used for this study, the calibration tests performed on the data acquisition system and the procedures used in sample handling and data acquisition. The apparatus description begins with the CO₂ laser followed by a description of the second harmonic generation set up, the optics external to the absorption cell, the absorption cell and the data acquisition system.

B. THE EXPERIMENTAL APPARATUS

1. The CO₂ Laser

The laser used in these experiments is an axial flow cw CO₂ laser which is grating tunable for single line operation. The output power for the laser lines used in the study varied from 2.5 to 3.0 watts. The grating can be tuned over both the 10.6 μm and 9.6 μm bands with output power greater than 1 watt for 25 and 22 lines, respectively. Table 3.1 shows the typical observed power for each of the lines.

TABLE 3.1

TYPICAL OUTPUT POWER FOR EACH CO₂ LASER LINE00°1 - 02°0 BAND 9.6 μ m

LINE	POWER (WATTS)	LINE	POWER (WATTS)
R(26)	1.1	P(10)	1.8
R(24)	1.9	P(12)	3.2
R(22)	2.8	P(14)	3.1
R(20)	2.6	P(16)	3.3
R(18)	2.8	P(18)	3.4
R(16)	2.1	P(20)	4.2
R(14)	2.3	P(22)	4.0
R(12)	1.2	P(24)	4.0
R(10)	1.3	P(26)	3.2
R(8)	0.9	P(28)	2.9
		P(30)	3.0
		P(32)	1.5
		P(34)	0.9
		P(36)	1.1

00°1 - 10°0 BAND 10.6 μ m

LINE	POWER (WATTS)	LINE	POWER (WATTS)
R(32)	0.9	P(6)	0.7
R(30)	1.5	P(8)	1.2
R(28)	2.2	P(10)	1.9
R(26)	3.2	P(12)	2.1
R(24)	2.9	P(14)	3.1
R(22)	3.1	P(16)	3.0
R(20)	3.8	P(18)	3.0
R(18)	3.0	P(20)	3.8
R(16)	2.5	P(22)	4.6
R(14)	3.0	P(24)	3.0
R(12)	2.8	P(26)	3.7
R(10)	2.0	P(28)	2.5
R(8)	1.1	P(30)	2.0
		P(32)	1.1
		P(34)	0.9

The resonant cavity for the laser that is shown schematically in Figure 3.1 consists of a flat grating, an adjustable iris, a ZnSe Brewster angle window and a ZnSe output window which is 60% reflecting at 10.6 μm and has a 5 meter radius of curvature. The output mirror is mounted on an adjustable piezoelectric-driven mount which provides sufficient length tuning of the cavity for optimal power output and open loop stability.

The resonant cavity stability condition is

$$0 < \left(1 - \frac{2L}{R_1}\right) \left(1 - \frac{2L}{R_2}\right) < 1 \quad (33)$$

where $L = 1.5$ meters, the cavity length; $R_1 = \infty$, the radius of curvature of the flat grating, and $R_2 = 5$ meters, which is the radius of curvature of the output mirror. Indeed, this cavity meets this condition as shown in Equation (34),

$$0 < 0.40 < 1 \quad (34)$$

Calculations of the beam waist at the grating and the spot size at the output mirror are shown in Equations (35) and (36),

$$\omega_0 = \omega_1 = \frac{L\lambda}{\pi} \left(\frac{g}{1-g}\right)^{1/4} = 2.78 \text{ mm} \quad (35)$$

$$\omega_2 = \frac{L\lambda}{\pi} \left(\frac{g}{g(1-g)}\right)^{1/4} = 3.04 \text{ mm} \quad (36)$$

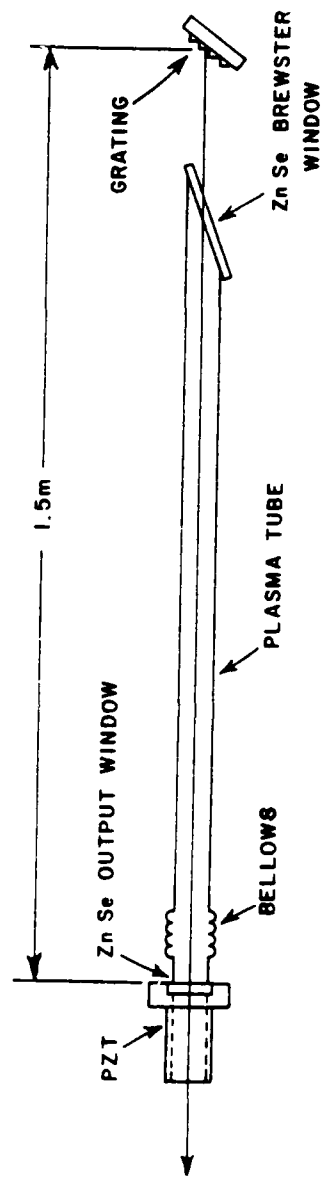


Figure 3.1 Schematic diagram of the laser optics and plasma tube.

where

$$g = 1 - \frac{L}{R_2} = 0.7$$

$$L = 1.5 \text{ m}$$

$$\lambda = 10.6 \text{ } \mu\text{m} \text{ .}$$

The iris was required in the cavity to insure single mode operation. The grating is tuned with a micrometer adjustment and has a relatively large dispersion which permits precise and reliable selection of the desired line.

The laser is an axial flow type of system containing a gas mixture of He-N₂-CO₂ with a partial pressure ratio of 80:10:10, respectively. The gas pressure at the inlet is typically 11.5 Torr. Tap water flows through an external jacket and serves to cool the gas flow. The laser discharge is excited by a Universal Voltronics model BAC 16-50 DC power supply connected in series to a forced air cooled 700 K Ω ballast resistor/capacitor bank. Typically, the DC voltage measured at the source is 13 KV with a 9 mA current.

The laser tube is supported by a 1.7 meter long Invar structure mounted to the steel base plate at the grating end only, with the other end resting in a sliding mount which allows for thermal linear expansion of the structure.

2. Second Harmonic Generation

The second harmonic generation was achieved by mounting a CdGeAs₂ crystal on the cold finger of a Janis research dewar model DT, cooling it down to 77K with liquid nitrogen, and then pumping the crystal with approximately 3 watts of cw radiation from the previously described CO₂ laser. Figures 3.2 and 3.3 show the crystal dewar and the CO₂ laser, respectively.

The CdGeAs₂ crystal, which is 3 x 5.5 mm in cross section and 6.4 mm long, was loaned to us by Dr. Dennis Killinger and Dr. Norman Menyuk of The Massachusetts Institute of Technology Lincoln Laboratory. This crystal is one of the most useful second harmonic generation materials for the infrared spectral region, since it has one of the highest non-linear coefficients known and a useful transmission range from 3 μ m to 17 μ m.

The optical absorption is decreased by cooling the crystal, with Lincoln Laboratory reporting 0.1 and 0.4 cm⁻¹ at 10 and 5 μ m, respectively, having been measured for their best samples [22]. Our crystal shows considerably higher absorption but generates the desired amount of second harmonic energy.

It was cut for Type-I phase matching, with a propagation angle of 32.5° from the optical axis. Figure 3.4 shows how the fundamental must be polarized and propagated into the crystal for phase matching with the desired second harmonic. The second harmonic emerges from the crystal polarized in the ordinary direction, that is, the polarization is perpendicular to the optical axis, whereas the incoming fundamental is

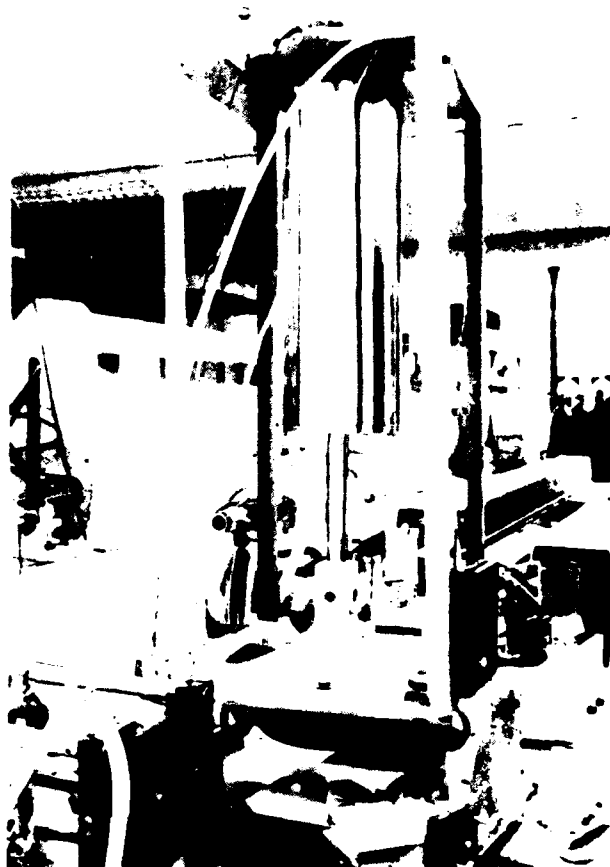


Figure 3.2 CdGeAs_2 crystal
liquid nitrogen
dewar.

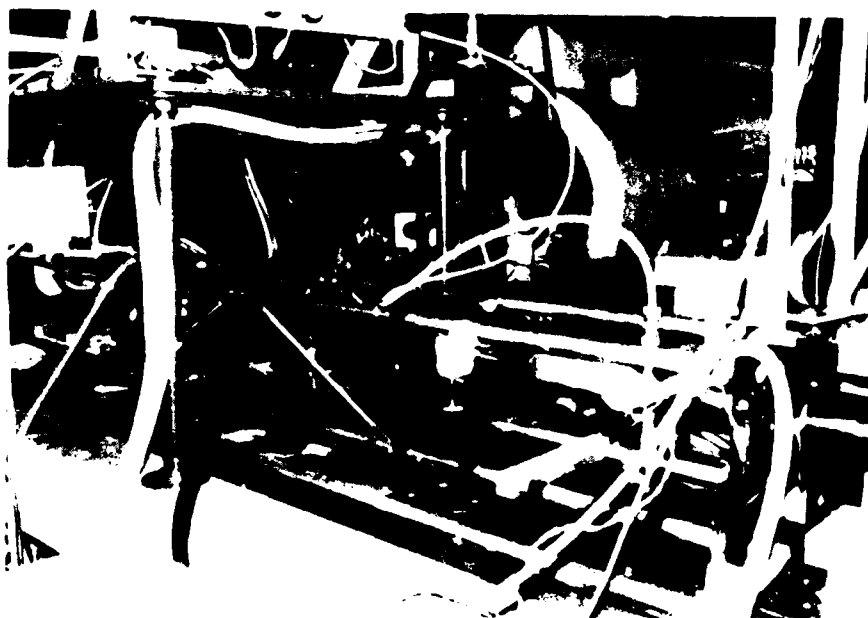


Figure 3.3 1.5 meter CO_2 laser.

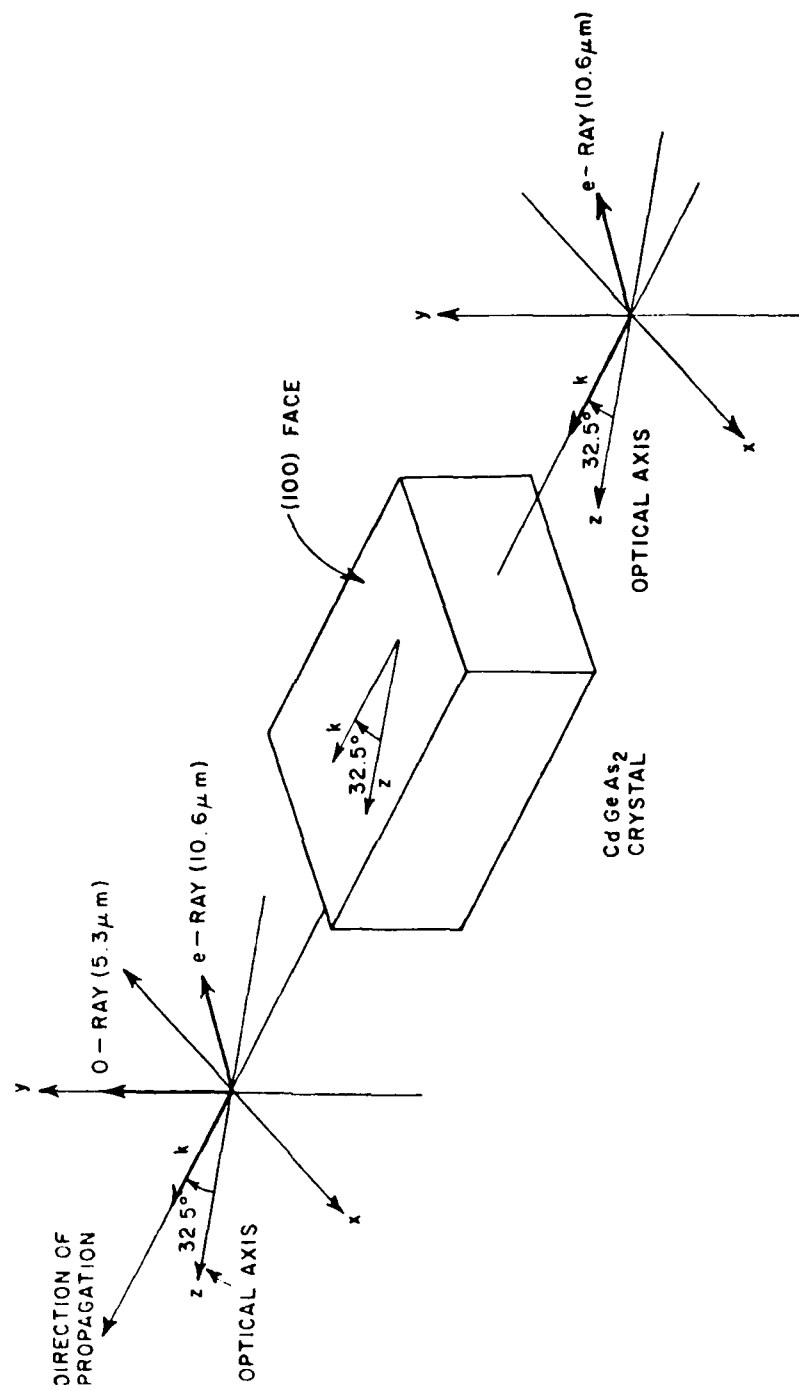


Figure 3.4 Polarization of input and output fields for second harmonic Type-I phase matching.

polarized in the extraordinary direction. One of the important properties of all nonlinear crystals is that their index of refraction varies as a function of both frequency and direction of propagation of the polarized radiation. These properties of birefringence and dispersion, respectively, are fundamental to second harmonic generation [23].

Figure 3.5 illustrates the elliptical characteristics of the index of refraction as a function of the spatial orientation of the direction of polarization for an electromagnetic wave propagating through a typical nonlinear crystal. For the extraordinary direction of polarization, an e-ray, the index changes elliptically between the value of the ordinary index n_o , when the wave normal is parallel to the optical axis, and the extraordinary index n_e , when the wave normal is perpendicular to the optical axis. Phase matching and therefore second harmonic generation is achieved when

$$n_{2\omega}^o = n_{\omega}^e(\theta) \quad (37)$$

where $n_{2\omega}^o$ = second harmonic o-ray index, and

n_{ω}^e = fundamental e-ray index as a function of θ .

Because the index of the fundamental e-ray can be varied by changing the angle between the optical axis and the wave normal, we are able to propagate the wave at an angle θ to the optical axis such that the refractive index for the input is exactly equal to the refractive index for the second harmonic. This angle is approximately $\theta = 35^\circ$ for $10.6 \mu\text{m}$ and thus is the reason for the crystal being cut as shown in

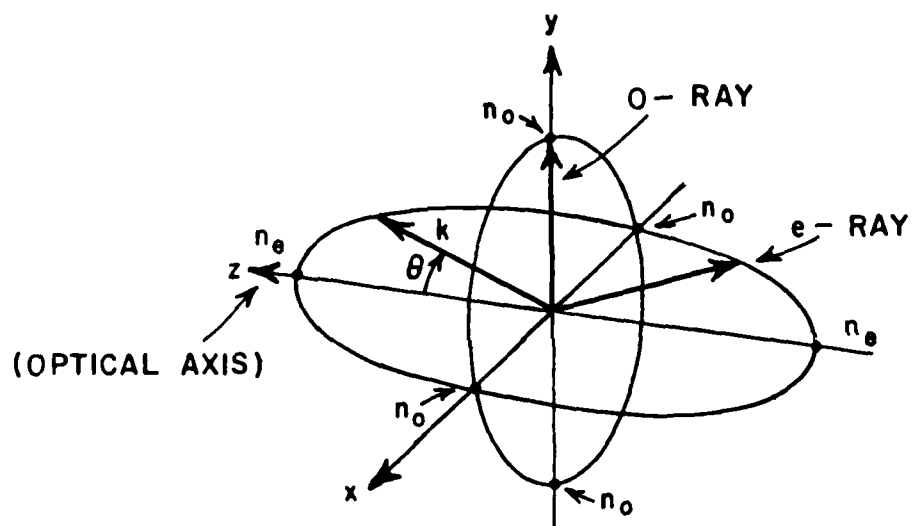


Figure 3.5 Illustration of the elliptical characteristics of the index of refraction as a function of the spatial orientation of polarization for an electro-magnetic wave propagating through a typical nonlinear crystal.

Figure 3.2. With the crystal cut in this way, the phase matched fundamental wave normal is nearly perpendicular to the crystal face.

The second concern in generating second harmonics is the fundamental beam intensity inside the crystal. It can be shown [23] that there is an optimum beam waist size for a given wavelength and crystal length in order to achieve the maximum second harmonic output power. This optimum beam waist size is obtained by setting $L = 6.4 \text{ mm}$ and $\lambda = 10.6 \text{ }\mu\text{m}$ in Equation (38),

$$\omega_0 = \frac{\left(\frac{L}{2.84}\right)\lambda}{2\pi} = 62.14 \text{ }\mu\text{m} . \quad (38)$$

The beam was focused in the crystal with a 30 cm radius of curvature spherical mirror. The spot size on the mirror was calculated to be $\omega = 4.15 \text{ }\mu\text{m}$ so the beam waist at the focus was calculated to be $\omega_0 = 121.95 \text{ }\mu\text{m}$ using Equation (39)

$$\omega_0 = \frac{f\lambda}{\pi\omega} = 121.95 \text{ }\mu\text{m} \quad (39)$$

where

$$f = R/2$$

$$R = 30 \text{ cm} .$$

This is roughly twice the optimum beam waist; however, the second harmonic power obtained with this intensity was sufficiently high for our purposes. In addition, focusing with the larger beam waist lowers the possibility of thermally damaging the crystal.

3. The External Optical System

The entire optical system, external to the absorption cell, is shown in Figure 3.6. Most of the 10.6 μm radiation is attenuated by a LiF_2 window mounted to the output window of the crystal dewar. This filtering, together with the sapphire windows on the detectors and their frequency response to 10.6 μm insure that the radiation measured during these experiments was the 5.3 μm second harmonic.

Other components of the external optical system include a Hughes Helium-Neon laser model 322H-PC (HeNe #1 of Figure 3.6), which was bore sighted with the CO_2 laser and allowed precise alignment of the CO_2 laser with the crystal and absorption cell optics, and a Spectra Physics Helium-Neon laser model 125 (HeNe #2) which served as the primary alignment laser for the absorption cell optics and detectors. The two irises were used to colinearize the two alignment lasers and thus align the second harmonics with the absorption cell and the detectors.

4. The 10.785 Meter Multipass Absorption Cell

The 24 inch diameter by 10.785 meter long multipass absorption cell used for this experiment was designed by Professor Edward K. Damon [15] and the unique optics system, shown in the top portion of Figure 3.6, which couples the laser and the interferometer to the optics of the absorption cell was designed by Dr. Robert J. Nordstrom. The 10.875 meter cell design is a significant improvement over the old 15.24 meter cell previously described [25,26] and used at The Ohio State University,

as well as the standard White type cell design [27]. The improved design allows for longer path lengths with improved spatial stability and reduced aberration effects.

The internal mirrors have a reflectivity of 98.6% at 10.6 μm and a radius of curvature of 10.785 meters. Figure 3.7 shows the spot arrangement on the field mirror of the cell. Spot 5 would typically be the output spot on a White type system but on this cell it is fed back into the optical system generating two additional rows of spots. Path lengths up to 1.8 Km are possible with laser sources and lengths of 1.0 Km have been achieved with broadband sources. The mirrors are adjusted by microprocessor controlled stepper motors thus allowing the path lengths to be easily changed.

Calculation of the path length is simply determined by considering that each spot, including spot 5 and the output spot, represents a round trip length of 21.570 meters. An additional 1.5 meters is added to account for the path lengths of the input and output periscope optics. The path length used for this study was 130.9 meters, where a column of four spots was seen on the field mirror plus spot 5 and the output spot.

Other features of the cell include a mounting system that rigidly couples the external optics to the cell but isolates both the external optics and the cell from any building vibration. The cell walls are constructed from 304 stainless steel with a very smooth interior to keep absorbance effects to a minimum. Buffer gases are introduced uniformly along the cell allowing for much faster sample mix times

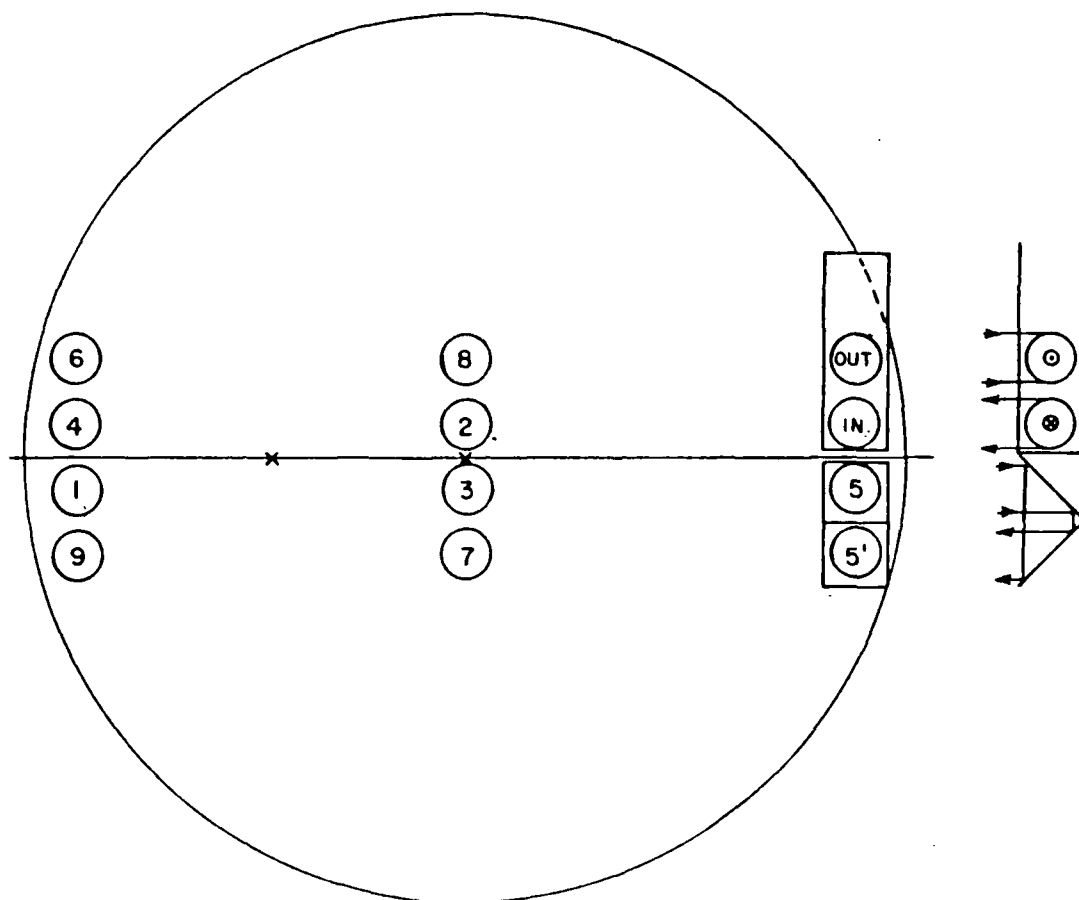


Figure 3.7 Example of spot pattern on field mirror for a path length of 217.2 meters.

than those of the old 15.24 meter cell. The vacuum system is a Kinney model KTC-112 compound vacuum pump which is capable of evacuating the entire cell in about 5 minutes. Another very important feature of this cell is that it can be temperature controlled from -60°C to $+60^{\circ}\text{C}$ with a uniformity of 2 C over the entire cell length.

5. The Computer Controlled Data Acquisition System

The data acquisition system used for this experiment consists of an IMSAI Model 8080 microcomputer, a teletype, a high speed 24 channel analog to digital converter, two DC amplifiers, two lock-in amplifiers, a pre-amp and filter unit, and two InSb detectors.

The two channels of the A/D are sampled 1024 times each with the channels being sampled 10 msec apart with a 50 msec delay between each pair of readings. The 1024 samples are divided into four groups of 256 each and after a group of 256 samples has been taken a printout is made of the average and standard deviation for each channel as well as the ratio of the two channels, i.e., Signal/Reference. This grouping allows the experimenter to observe any trends in the data. The averaging tends to filter out any signal variations due to 120 Hertz line ripple, room vibration, or laser power fluctuations.

Figure 3.8 shows a block diagram of the data acquisition system. The A/D unit is a 12 bit Altair A/D with 2.5 mV resolution, measuring from 0 to 9.9974 volts. Ectron model R516-6A DC amplifiers were used to amplify the analog signals coming out of the lock-in amplifiers.

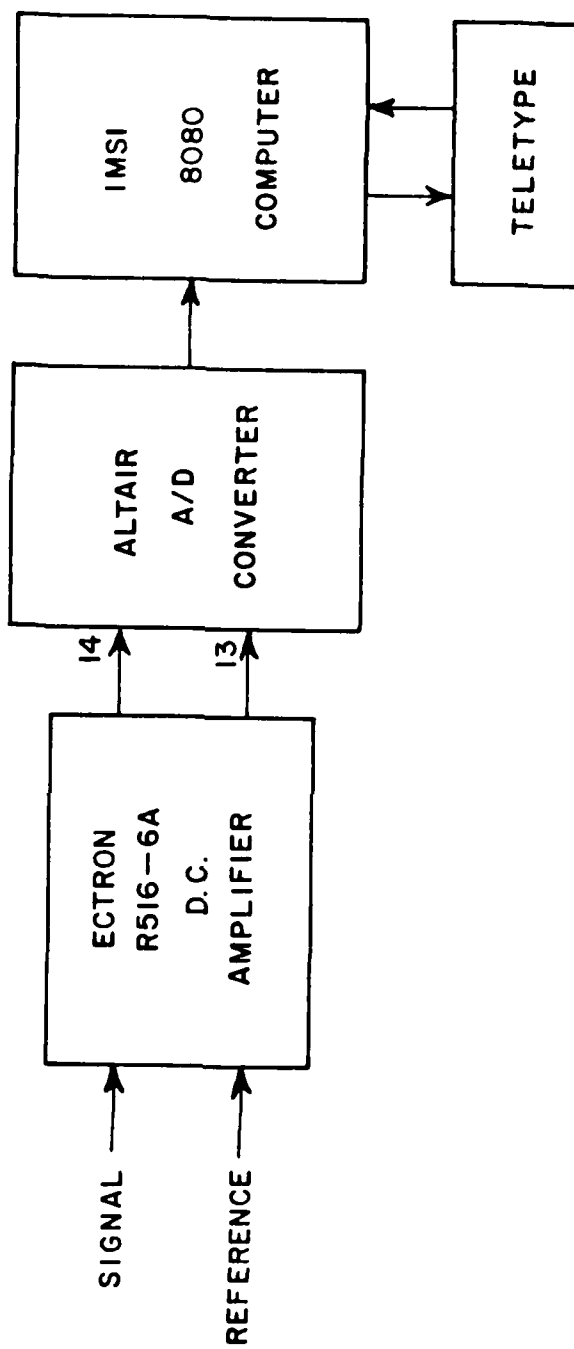


Figure 3.8 Block diagram of data acquisition system.

Their output signal ranges from 0 to 1 volts so the DC amps were set to a gain of 10 to boost the signal levels to between 0 and 10 volts to the A/D unit. The calibration of the system is discussed in Section C.

Princeton Applied Research model 128A lock in amplifiers were used in this data acquisition system to synchronously detect and integrate the signal from each detector. A radiation chopper, Laser Precision model CTX-534, provided 100% modulation of the second harmonic into the detectors and has its external synchronizing line connected to the phase reference input of the lock in amplifiers.

Specifically, the lock in amplifiers provide accurate voltage measurement for signals corrupted by broad band noise and power line pick up, for example. An extremely narrow band synchronous detector, whose passband center is locked in with the chopper frequency provides an excellent signal to noise ratio. The input selectivity range can be varied from 1 V to 250 mV full scale. The analog output has an adjustable low pass filter which can be used to damp out fluctuations from the synchronous detector stage.

InSb detectors are excellent for detection of small signal radiation in this spectral region for their frequency response peaks at about 4.6 μm which is close to the 5.3 μm second harmonic radiation. The signal detector, a Judson model J-10 nitrogen cooled InSb detector, is photovoltaic and thus requires no biasing circuitry. Its output was connected directly to the signal channel lock in amplifier. The reference detector, an Infrared Associates model DNSL- 18 Hrs. nitrogen

cooled InSb detector, is also photovoltaic. However, because of the very low intensity of the reference beam after reflection from a BaF₂ wedge, it was found that a better signal to noise ratio could be obtained by connecting the detector to a Nicolet FTIR pre-amp and filter unit and then to the reference channel lock-in amplifier.

C. TESTS

1. DC Amplifier and A/D Calibration

The Ectron DC amplifiers and the Altair A/D were tested and calibrated by feeding the output from an Analogic model AN 3100 voltage standard with a resolution of 0.1 millivolts into each DC amplifier and incrementing the voltage from 0.05 to 0.95 volts by 0.05 volt steps. The output from the amplifiers was read at each step by the A/D and computer. Since the gain of the amplifiers was 10 the theoretical output was from 0.5 volts to 9.5 by 0.5 volt increments. This theoretical value was compared with the value actually read and the error (=output - theoretical) was plotted and is displayed in Figure 3.9. This error is very small and averages to less than 0.4% across the entire voltage range. Since the signal channel reading is divided by the reference channel and the signal and reference calibration curves track with each other so closely, this error is almost completely cancelled out in the data measurements.

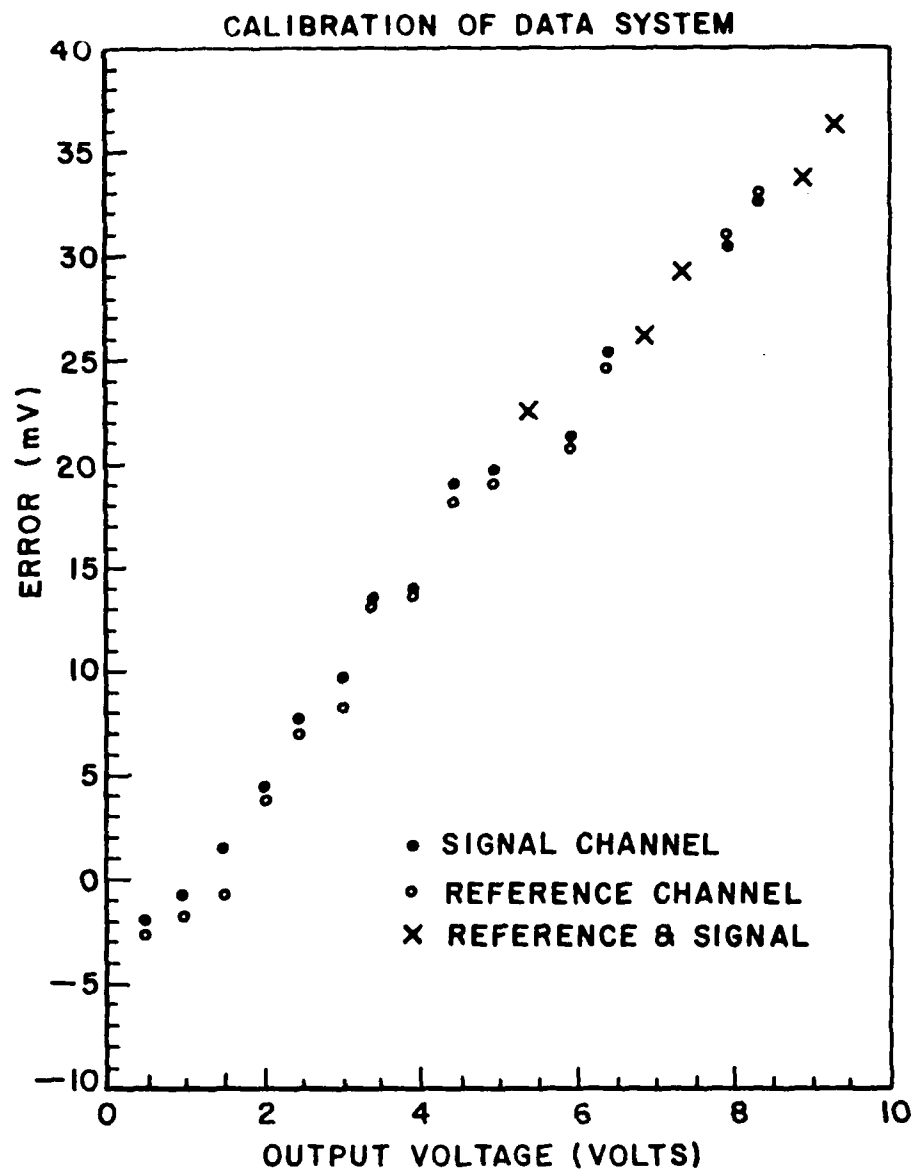


Figure 3.9 Calibration data for the signal and reference channels.
The error in mV is plotted versus theoretical output.

2. The Lock-in Amplifiers

Both of the lock-in amplifiers had been recently calibrated and tested in a previous study [26] and so only a few non-rigorous tests were conducted. A continuity check was made between the different sensitivity scales, a rough calibration check was made using a sinusoidal input, and the lock-in amplifiers were also checked for reference detector phase drift. All of the above mentioned tests indicated that the amplifiers were still performing quite well.

D. EXPERIMENTAL PROCEDURES

1. Introduction

This section discusses the general procedures used to align the optical system, get the proper amount of sample in the absorption cell, and to acquire the data. In addition, various technical difficulties encountered throughout the experiment will be discussed.

2. Optical Alignment

Much of this discussion refers to Figure 3.6. Initially the large HeNe #2 shown in Figure 3.6 was used to align the absorption cell optics and to set the number of passes through the cell to six for a path length of 130.9 meters. Then HeNe #2 was used to align the signal and reference detectors for optimum response. Next, with the CdGeAs₂ crystal temporarily moved out of the optical path, the HeNe #1 laser

(Figure 3.6) which is boresighted with the CO₂ laser was colinearized with HeNe #2 through the use of Iris 1 and 2 and adjustment of mirrors A and B. At this point the detector alignment was rechecked using HeNe #1.

The crystal was then moved back into the optical path using HeNe #1 to target the crystal. The crystal had to be targeted with liquid nitrogen already in the crystal dewar because the rod that the crystal was mounted on inside the dewar would contract by approximately 2 millimeters during the initial cooling down to the operating temperature of 77°K. Once the crystal was in place, the CO₂ laser was turned on and the second harmonics were tuned in by translating and rotating the entire crystal dewar assembly. In addition, the crystal could be vertically adjusted by a pedestal which the dewar rested on. This pedestal had to be abandoned later due to the fact that thermal expansion and contraction of the dewar's outer skin vertically disoriented the crystal and so the dewar had to be suspended to null these effects. After a sufficient amount of second harmonics had been tuned in by crystal reorientation, mirrors A and B were again used to recheck and correct the detector alignment for optimum response.

3. Background Measurements

After establishing a sufficient amount of second harmonic (i.e., 2.5 mv reading from the signal detector), a 100% transmittance level or background would be measured. Equation (39) shows the formula used to obtain the transmittance measurements,

$$T = \frac{I_S(n)/I_{RS}}{I_B(n)/I_{RB}} \quad (40)$$

T = transmittance

$I_S(n)$ = attenuated intensity level due to the sample

I_{RS} = reference detector signal level during sample
measurement

$I_B(n)$ = unattenuated intensity level (signal background)

I_{RB} = reference detector signal level during signal background
measurement

n = number of traversals.

Thus, as Equation (40) indicates, a $I_B(n)/I_{RB}$ background must be known in order to obtain the transmittance.

A stable background is very important for obtaining accurate data but unfortunately the background measurements for this experiment were quite often unstable. The instability was tolerable during data acquisition at the first two temperatures of 295°K and 310°K but became too unreasonable to work with during data acquisition at the third temperature of 323°K. Thus, the data gathered for the first temperatures can be taken with a fair amount of confidence but the data at $T = 323^\circ\text{K}$ is in need of much verification.

The source of the instability was never fully determined although a couple of revealing observations were made near the end of the study when the background could not be stabilized at all. First it was discovered that a stable background could not even be obtained by just using the HeNe #1 laser as the source (independent of the CO₂ laser and

the crystal). When the Judson J-10 signal detector was replaced by a HgCdTe (12 μ m peak) detector, a stable background was then able to be measured using HeNe #1. However, when just the CO₂ laser was reintroduced into the system (i.e., no second harmonic generation) with the new signal detector, the background was again unstable although not nearly as much. This seemed to indicate that the CO₂ laser was a source of instability also; although it was never determined how it could cause such instability. In any case, a sufficient amount of data was obtained at the two lower temperatures when the system was relatively stable.

4. Sample Handling

The water samples were loaded into the cell by first filling a pyrex glass container which was vacuum coupled to the side port of the absorption cell, and then heating the container with a heat gun, thereby allowing the water to evaporate into the cell. The desired partial pressure of the water was established by measuring into the sample container the volume of water required to get the desired pressure for some known temperature and volume of the cell in accordance with the ideal gas law. Table 3.2 lists the water volumes used for the various sample pressures and temperatures investigated. Once the sample was in the cell, it was nitrogen broadened to a total pressure of 740 Torr. This pressure was chosen so that the cell would have a slight negative pressure, for which the cell seals were designed, and thus a stable total pressure could be maintained throughout the transmittance measurement.

TABLE 3.2
H₂O SAMPLE VOLUMES REQUIRED TO ESTABLISH PARTIAL PRESSURE
OF 5, 10, AND 15 TORR AT TEMPERATURES OF
295°K, 310°K AND 323°K

H ₂ O Partial Pressure (Torr)	T = 295°K Volume (ml)	T = 310°K Volume (ml)	T = 323°K Volume (ml)
5	16.8	16.0	15.3
10	33.6	31.9	30.6
15	50.3	47.9	45.9

5. Transmittance Measurements

Once the nitrogen broadened sample was in the cell and the desired temperature established, several readings were taken for each of the three laser lines of interest. If the readings appeared to be slightly unstable, measurements were taken until a stable plateau was observed and then the cell quickly pumped down to obtain a background measurement. On the other hand, if the readings appeared fairly stable for a 10 Torr sample partial pressure, for example, the cell would be pumped down to just 370 Torr and refilled with nitrogen to 740 Torr. This would cut the partial pressure of the sample to 5 Torr and another set of transmittance readings would be obtained. In any case, a final

empty cell background was always measured. The absorption coefficients were then determined using Equation (40) and Equation (41) where two absorption coefficient measurements would be determined.

$$K = \frac{\ln T}{.1309} \text{ (km}^{-1}\text{)} \quad (41)$$

where

T = transmittance

.1309 = path length in km.

The first measurement used the transmittance based on the first background obtained for introduction of the sample into the cell and the second used the transmittance based on the final background reading. These two readings make up the end points of the error bars shown in the data plots (Figures 4.1 through 4.9). Although the coefficient obtained by using the final background reading may in some cases be more accurate due to the shorter time interval between sample and background readings, the same weighting was given to each end point when the curve of best fit was determined.

CHAPTER IV

DATA ANALYSIS

A. INTRODUCTION

Measurements of nitrogen-broadened water vapor absorption made at temperatures of 296°K, 310°K and 323°K are presented in this chapter for three frequency doubled CO₂ laser lines. The first section discusses the line selection criteria used in selecting the investigated frequencies as well as a word about the temperature selection. Then the data is presented and compared to the theoretical absorption predicted by the TN model.

B. SELECTION OF THE INVESTIGATED FREQUENCIES, TEMPERATURES AND PRESSURES

This study investigated the nitrogen broadened water vapor absorption for three CO₂ laser lines:

- 1) $2\nu[R(12)] = 1941.0958 \text{ cm}^{-1}$
- 2) $2\nu[R(14)] = 1943.8618 \text{ cm}^{-1}$
- 3) $2\nu[R(18)] = 1949.2452 \text{ cm}^{-1}$.

The above lines are from the ($00^\circ 1 - 10^\circ 0$) $10.6 \mu\text{m}$ band of the CO_2 laser and were frequency doubled by the CdGeAs_2 crystal described in Chapter III.

Because the primary intent of the study was to observe the line shape behavior of local lines where the continuum absorption was of little significance, these lines were chosen on the basis of their locations relative to the line centers of local absorption lines. Due to a lack of 740 torr nitrogen broadened spectral data in this region, the selection was based, in part, on the pure water vapor spectra shown in Figures 4.1a and 4.1b. Table 4.1 indicates the different temperatures and pressures for which each of the four rows of spectra were recorded. The second row (Row B) best approximates the pressure and temperature range of the study. Observe that the $2\nu[\text{R}(12)]$ and the $2\nu[\text{R}(14)]$ lines lie somewhere in the intermediate to near line center regions of the local absorption lines. The intermediate wing of the absorption line shape has the least known about it theoretically, as was mentioned in Chapter II, and little is known about this region experimentally as a function of temperature. Therefore, these two laser lines are of great interest.

Pressure broadened spectra in this region does need to be recorded to verify the position of these two lines relative to the neighboring local absorption lines because it is uncertain just exactly where these two laser lines sit on the local line shapes. The $2\nu[\text{R}(12)] = 1941.0958 \text{ cm}^{-1}$ line is 0.5332 cm^{-1} away from a strong line at $1941.6290 \text{ cm}^{-1}$. If we assume that the pressure broadened line width

TABLE 4.1

EXPERIMENTAL CONDITIONS FOR THE PURE H₂O SPECTRA

SHOWN IN FIGURES 4.1a AND 4.1b

(PATH LENGTH = 821 METERS)

ROW OF FIGURE	T (°K)	H ₂ O PRESSURE (TORR)
A	284.4	5
B	295.3	10
C	307.1	20
D	320.2	40

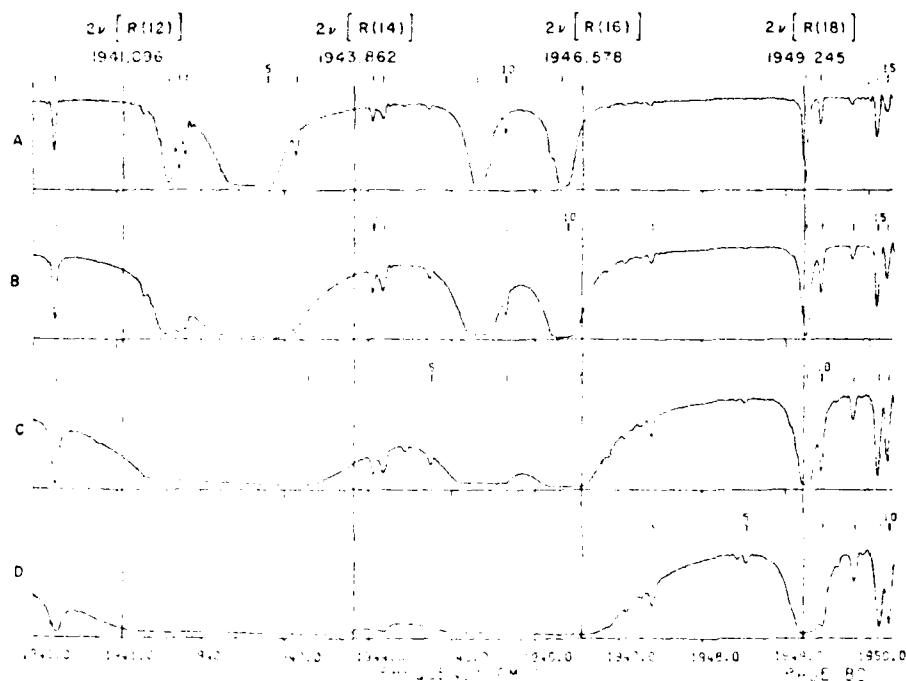


Figure 4.1a. Location of laser lines $2\nu[R(12)]$, $2\nu[R(14)]$, $2\nu[R(16)]$ and $2\nu[R(18)]$ in the spectral region under investigation. Table 4.1 describes the experimental conditions under which each row of spectra was recorded.

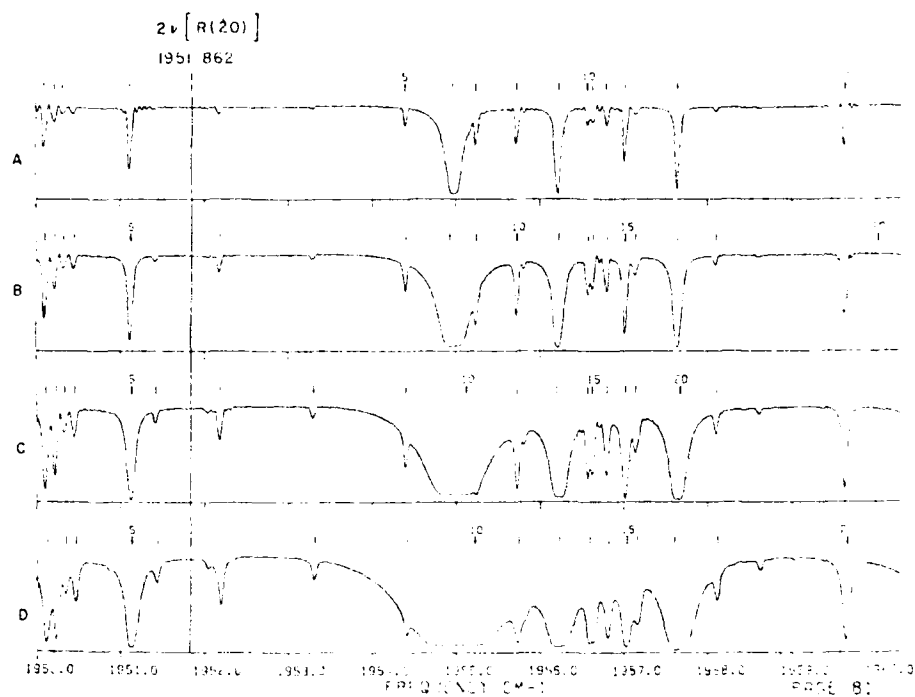


Figure 4.1b. Location of the laser line $2\nu[R(20)]$ in the spectral region under investigation. Table 4.1 describes the experimental conditions under which each row of spectra was recorded.

to be five times [28] the AFGL line width listing, then the $2\nu[R(12)]$ is 1.38 line widths away from line center. The $2\nu[R(14)] = 1943.8618 \text{ cm}^{-1}$ line is 1.3448 cm^{-1} away from a very strong line centered at $1942.5170 \text{ cm}^{-1}$. Using the same assumption as above, the $2\nu[R(14)]$ line is estimated to be 5.75 line widths from line center.

As for the $2\nu[R(18)] = 1949.2452 \text{ cm}^{-1}$ line, there is no doubt that it is well within the line width of a local line centered at $1949.2500 \text{ cm}^{-1}$. In fact, it is 0.014 line widths away from line center using the above line width criterion of 5 times the AFGL line width listing. This line should give an opportunity to observe the near line center shape as a function of temperature and pressure.

Another laser line in this region, the $2\nu[R(20)] = 1951.8622 \text{ cm}^{-1}$ shown in Figure 4.1b, is also of interest because it could possibly be paired with the $2\nu[R(18)]$ line as an on-line/off-line ($2\nu[R(18)]/2\nu[R(20)]$) resonant pair for use in differential lidar remote sensing of atmospheric water vapor. At least one frequency doubled CO_2 DIAL system is currently being developed [21] and the characteristics of this pair may be of interest and thus should be investigated further. In addition, these two lines appear to be off line resonance of the CO_2 molecule which can often be a problem in the near infrared region.

Observations of these lines were made for three temperatures, 295°K , 310°K , and 323°K . The 323°K temperature is as high as the safe operating upper limit of the absorption cell insulation. Temperatures lower than room temperature are also of interest but this study chose

to focus on room temperature and above.

The water vapor partial pressures were generally 5, 10 and 15 torr. Several data points at 295°K were taken with water vapor pressures slightly different than the three listed above due to an error in selecting the proper volume of H₂O samples to evaporate into the cell. The error was detected after the absorption measurements were taken and the actual pressures had to be recalculated and are believed to be correct for those particular measurements at 295°K.

C. DATA PRESENTATION AND ANALYSIS

1. Data Presentation

Tables 4.2 through 4.4 present the experimentally measured absorption coefficients as a function of water vapor pressure for the investigated laser lines and temperatures. Along with the data are the theoretical absorption coefficient values determined by use of the TN model. Both the experimental and theoretical values are plotted for each laser line and temperature in Figures 4.2 through 4.10.

The error bars in Figures 4.2 through 4.10 result from a shift in the measured background (or 100% transmittance level) during the experiment. One of the end points of each error bar represents the absorption coefficient value based on the initial background measurement and the other is based on the final background measurement, after the sample has been evacuated from the cell. As discussed in

TABLE 4.2
NITROGEN BROADENED H₂O ABSORPTION DATA GATHERED FOR THE
2ν(R(12)) = 1941.096 cm⁻¹ CO₂ LASER LINE

H ₂ O* p _a	Theoretical k(km ⁻¹)	Experimental k(km ⁻¹)	Temperature (°k)
5.4	5.0546	5.5680 - 5.8765	295
8.1	7.7285	7.7529 - 8.3540	295
10.0	9.6686	10.1480 - 10.8090	295
16.1	16.2226	16.1225 - 16.7310	295
5.0	4.7765	5.3859 - 5.4317	310
10.0	9.8850	10.8751 - 11.4873	310
15.0	15.3243	17.0015 - 17.2309	310
5.0	4.8561	-	323
10.0	10.0411	7.8369 - 9.0587	323
15.0	15.5540	-	323

*All samples nitrogen broadened to 740 Torr total pressure.

TABLE 4.3
NITROGEN BROADENED H₂O ABSORPTION DATA GATHERED FOR THE
2ν(R(14)) = 1943.862 cm⁻¹ CO₂ LASER LINE

H ₂ O* Pa	Theoretical k(km ⁻¹)	Experimental k(km ⁻¹)	Temperature (°K)
5.4	5.1312	6.1589 - 6.2922	295
8.1	7.8440	8.6566 - 9.5165	295
10.0	9.8117	11.1056 - 11.5271	295
16.1	16.4561	17.0808 - 17.9375	295
5.0	4.6333	5.4146 - 5.7333	310
10.0	9.5895	11.3992 - 12.2251	310
15.0	15.3243	16.7991 - 17.1013	310
5.0	4.5324	4.2527 - 4.6338	323
10.0	9.3760	7.1591 - 7.9797	323
15.0	14.5298	- -	323

*All samples nitrogen broadened to 740 Torr total pressure.

TABLE 4.4
NITROGEN BROADENED H₂O ABSORPTION DATA GATHERED FOR THE
2ν(R(18)) = 1949.245 cm⁻¹ CO₂ LASER LINE

H ₂ O* Pa	Theoretical k(km ⁻¹)	Experimental k(km ⁻¹)	Temperature (°K)
5.4	6.0398	6.5052 - 7.0831	295
8.1	9.8044	10.1327 - 10.8879	295
10.0	12.1183	12.0633 - 12.6428	295
16.1	19.5762	18.4152 - 19.2715	295
5.0	7.5425	8.1124 - 8.6830	310
10.0	15.1128	15.8347 - 16.8073	310
15.0	22.7013	23.3303 - 23.6706	310
5.0	8.9802	- -	323
10.0	18.0330	16.5227 - 17.1635	323
15.0	27.0681	- -	323

*All samples nitrogen broadened to 740 Torr total pressure.

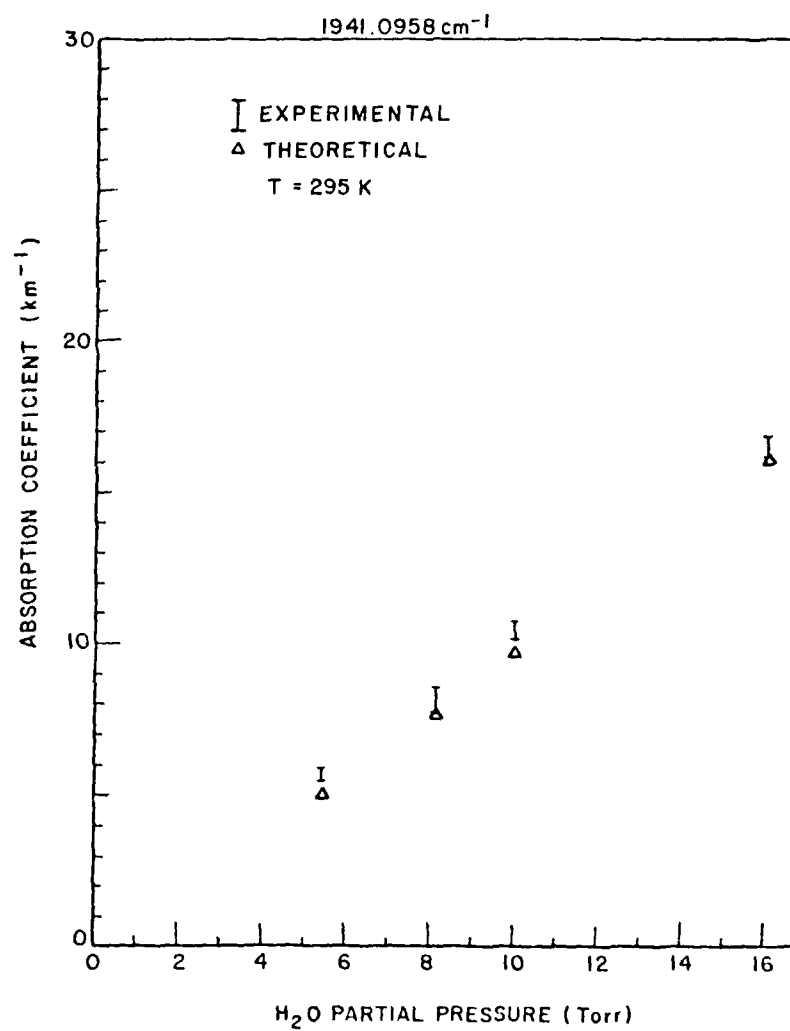


Figure 4.2 Comparison of experimental and theoretical H₂O partial pressure dependence for $2\nu[\text{R}(12)] = 1941.0958 \text{ cm}^{-1}$ at 295 K°.

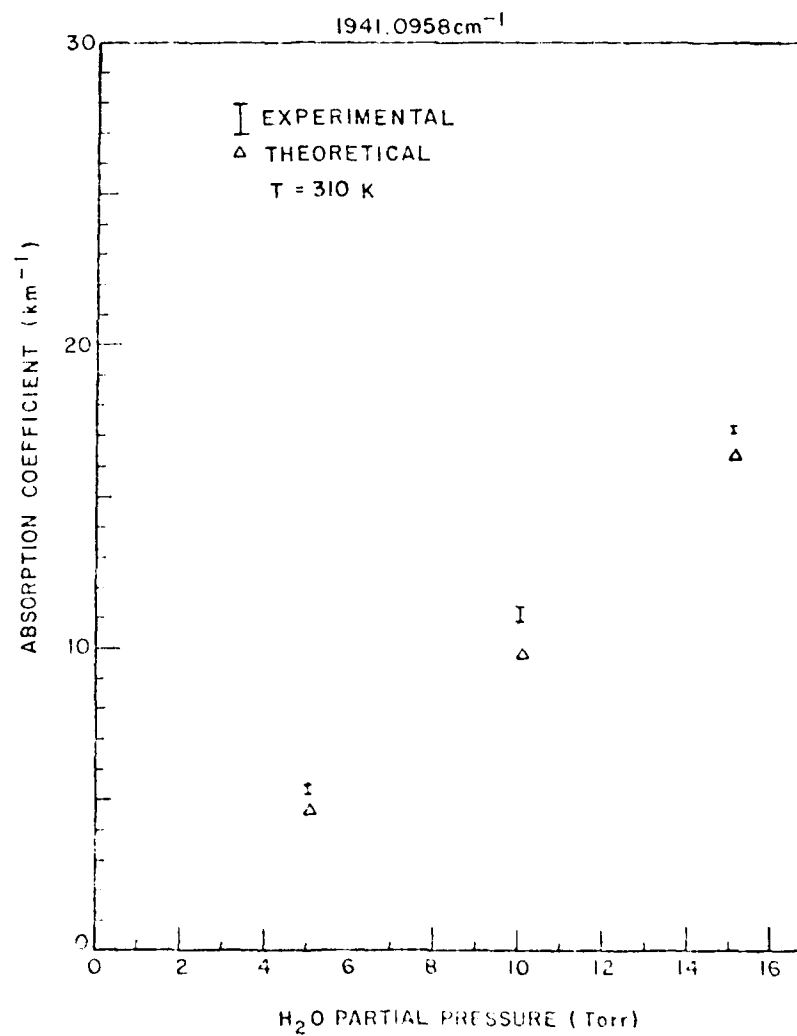


Figure 4.3 Comparison of experimental and theoretical H₂O partial pressure dependence for $2\nu[R(12)] = 1941.0958\text{ cm}^{-1}$ at 310 K^o.

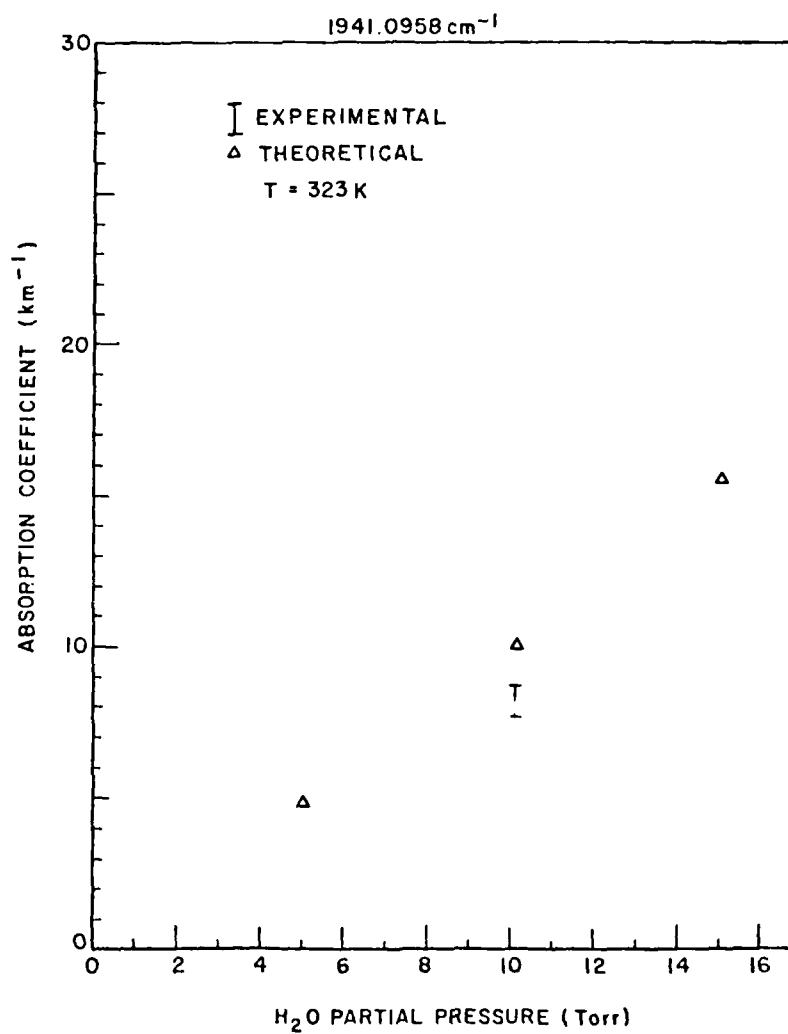


Figure 4.4 Comparison of experimental and theoretical H₂O partial pressure dependence for $2\nu[\text{R}(12)] = 1941.0958 \text{ cm}^{-1}$ at 323 K°.

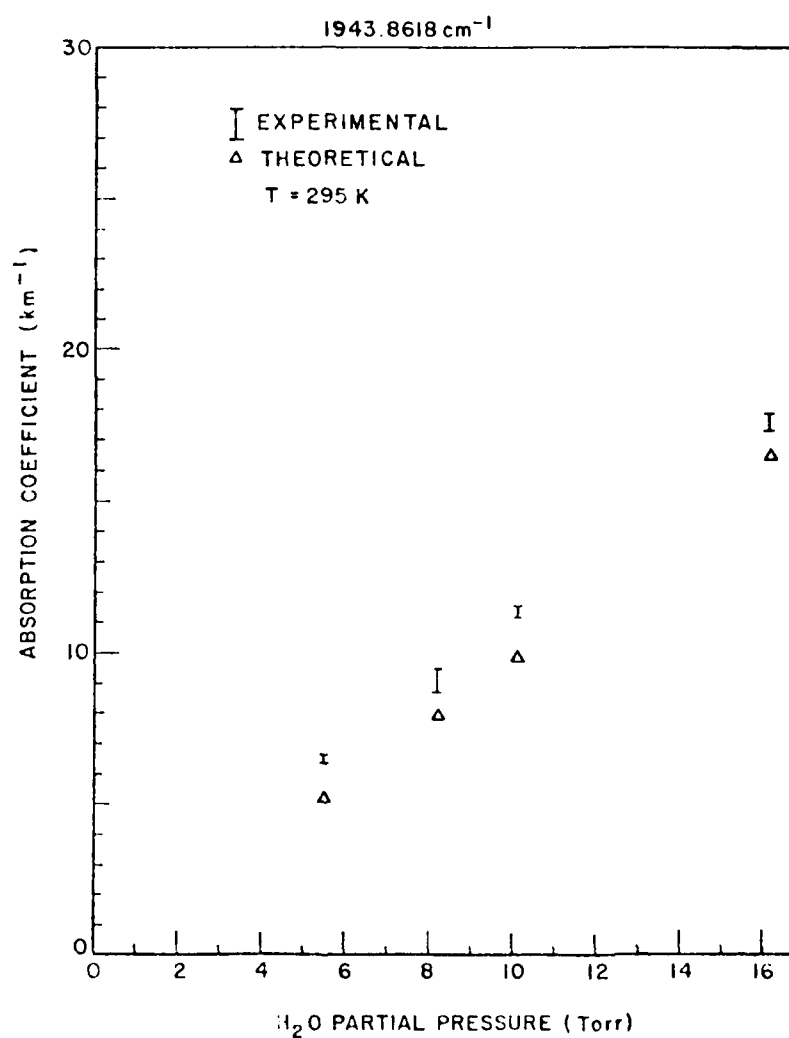


Figure 4.5 Comparison of experimental and theoretical H₂O partial pressure dependence for $2\nu[\text{R}(14)] = 1943.8618\text{ cm}^{-1}$ at 295 K.

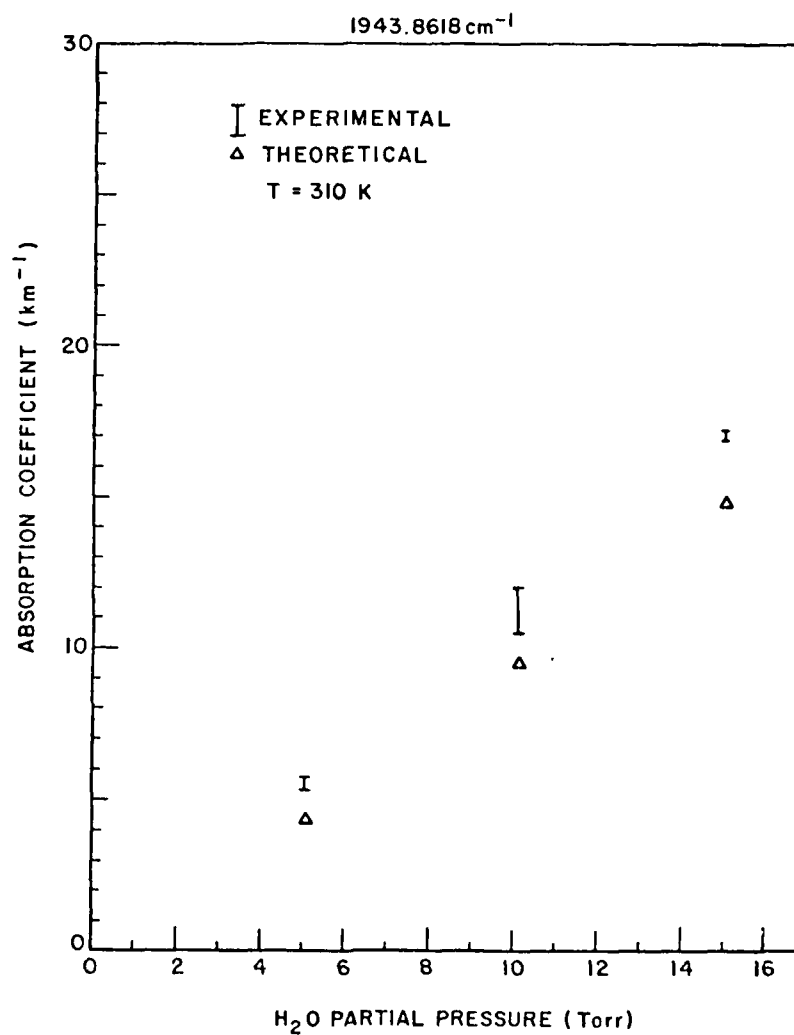


Figure 4.6 Comparison of experimental and theoretical H₂O partial pressure dependence for $2\nu[R(14)] = 1943.8618\text{ cm}^{-1}$ at 310 K°.

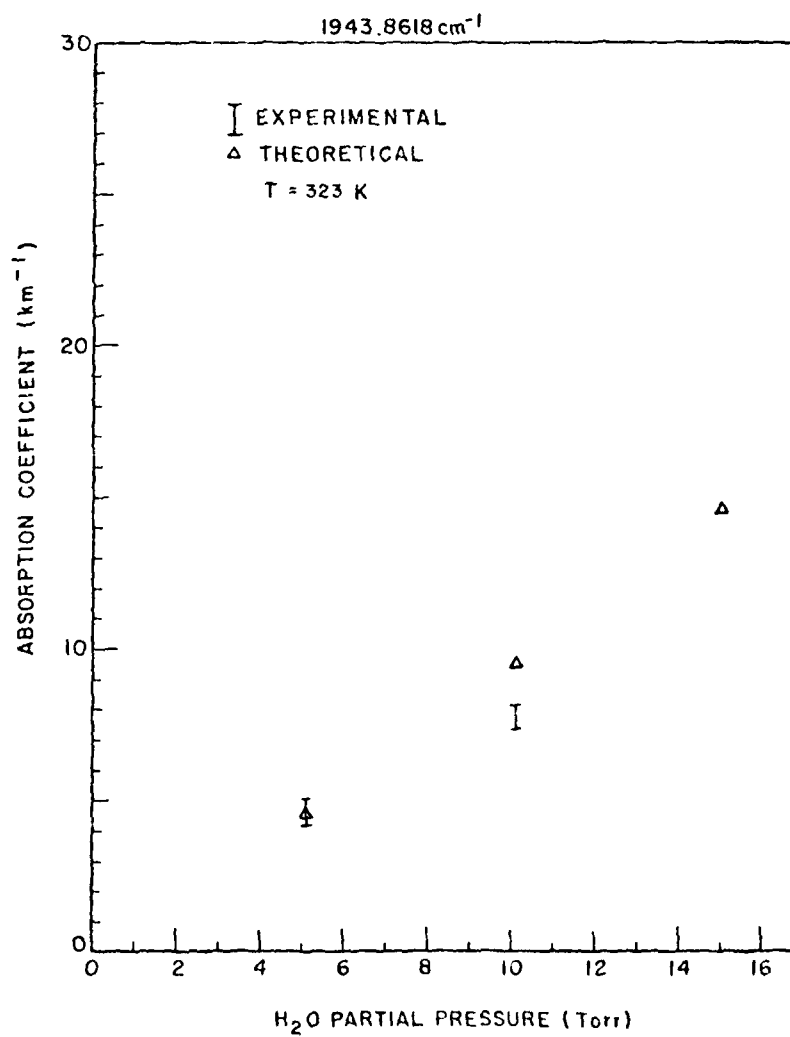


Figure 4.7 Comparison of experimental and theoretical H₂O partial pressure dependence for $2\nu[\text{R}(14)] = 1943.8618 \text{ cm}^{-1}$ at 323 K°.

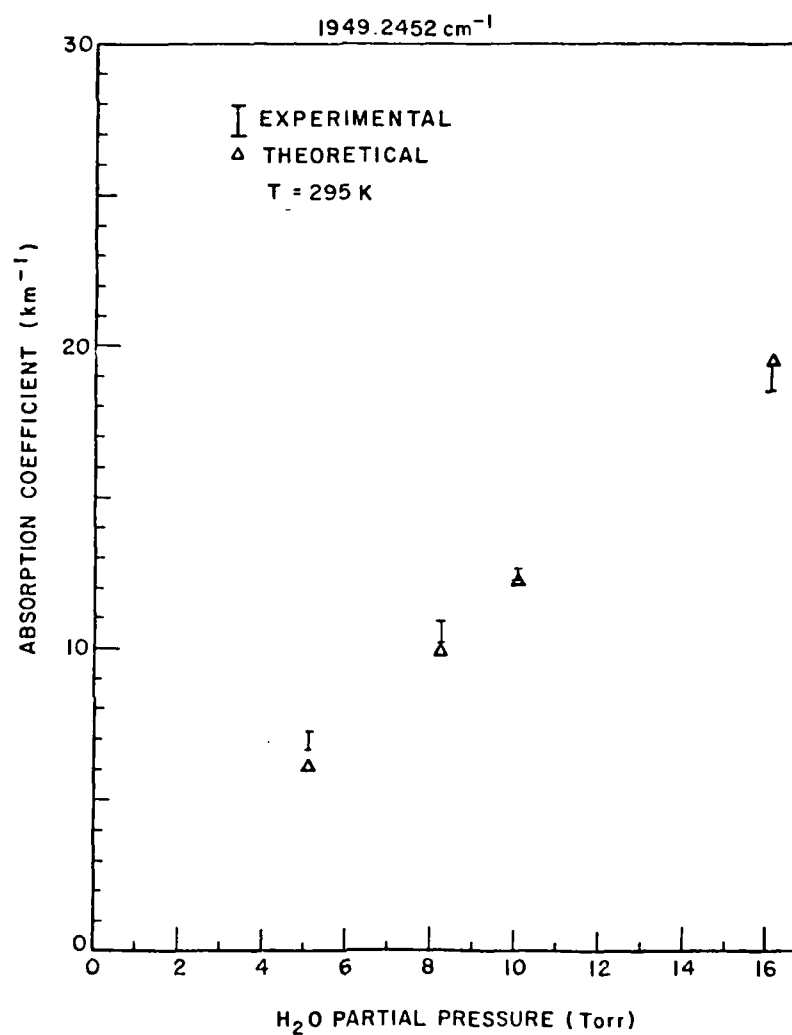


Figure 4.8 Comparison of experimental and theoretical H_2O partial pressure dependence for $2\nu[\text{R}(18)] = 1949.2452 \text{ cm}^{-1}$ at 295 K° .

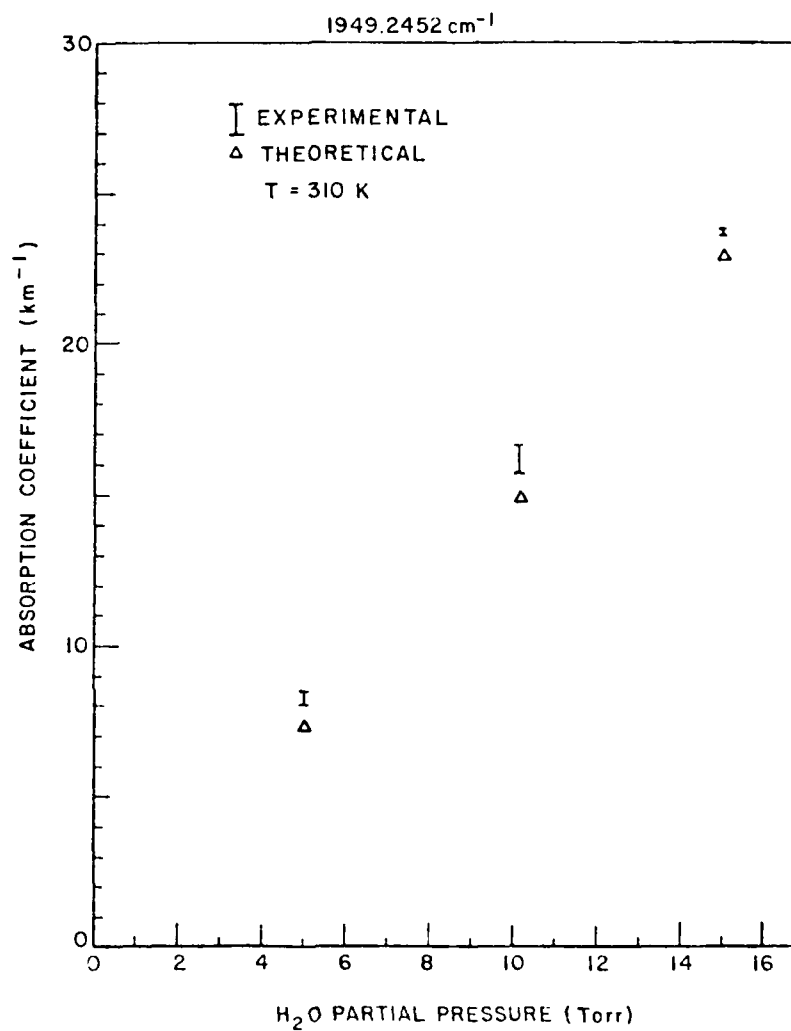


Figure 4.9 Comparison of experimental and theoretical H₂O partial pressure dependence for $2\nu[\text{R}(18)] = 1949.2452 \text{ cm}^{-1}$ at 310 K°.

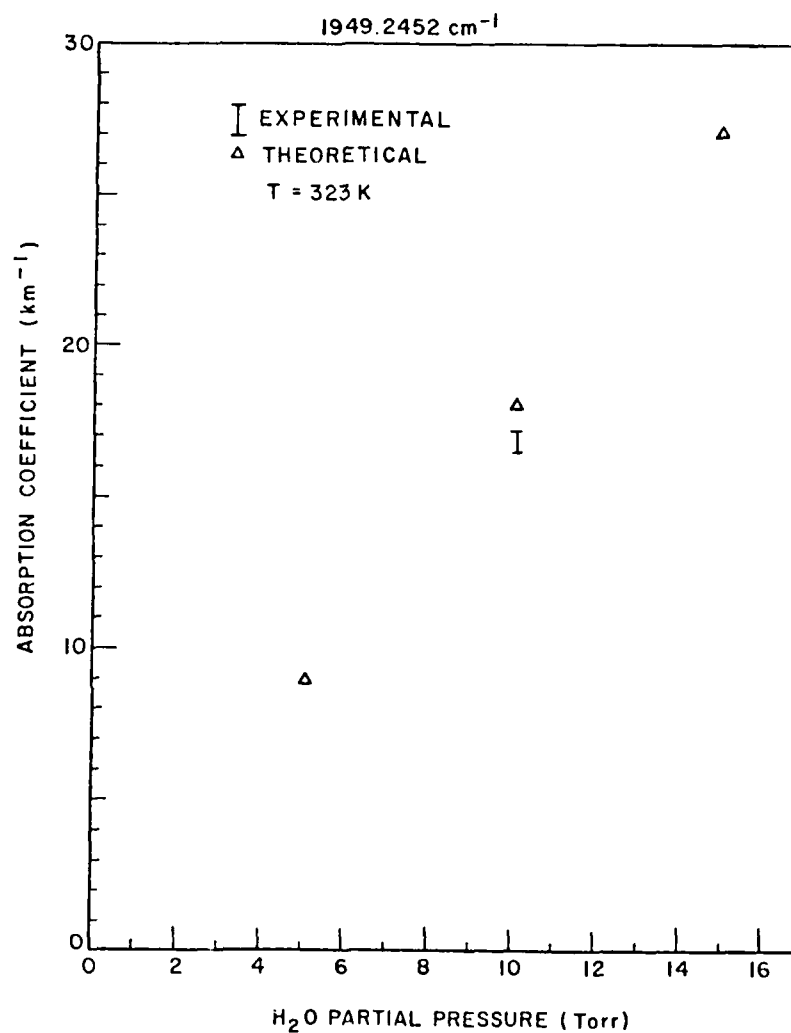


Figure 4.10 Comparison of experimental and theoretical H_2O partial pressure dependence for $2\nu[\text{R}(18)] = 1949.2452 \text{ cm}^{-1}$ at 323 K°.

Chapter III, establishing a stable background was the major and virtually unresolved problem encountered throughout the study. The problem finally got so dominant that only a small amount of data was able to be obtained at 323°K. The data that was obtained at the $2\nu[R(12)]$ and $2\nu[R(18)]$ lines is questionable and cannot be taken with much confidence. Data measured for 295°K, 310°K and the $2\nu[R(14)]$ line at 323°K is believed to be more accurate but the instabilities of the system greatly de-sensitized all of the absorption measurements.

2. The Empirical Expression for the Absorption Coefficient

The general form of the absorption coefficient which is used to express the data is

$$k(\nu) = \frac{p_a}{RT} (p_{N_2} C_N + p_a C_S) [\text{km}^{-1}] \quad (42)$$

where C_S is the self-broadening coefficient for water vapor, C_N is the nitrogen broadening coefficient, p_{N_2} is the pressure of nitrogen in torr, p_a is the water vapor partial pressure in torr, R is the ideal gas constant, and T is the temperature in Kelvin. For this data, the following expression is also true:

$$p_T = p_{N_2} + p_a = 740 \text{ torr} . \quad (43)$$

Substituting for p_N in Equation (42) yields,

$$k(\nu) = \frac{p_a}{RT} ((p_T - p_a) C_N + p_a C_S) [\text{km}^{-1}] \quad (44)$$

$$k(\nu) = \left(\frac{p_T C_N}{RT}\right) p_a + \left(\frac{C_S - C_N}{RT}\right) p_a^2 [\text{km}^{-1}] . \quad (45)$$

Thus, a general second order polynomial can represent the data,

$$k(\nu) = A p_a + B p_a^2 [\text{km}^{-1}] , \quad (46)$$

where

$$A = \frac{p_T C_N}{RT} [\text{km}^{-1} \text{ torr}^{-1}]$$

$$B = \frac{C_S - C_N}{RT} [\text{km}^{-1} \text{ torr}^{-2}] .$$

This expression is valid for absorption coefficients at frequencies further than one line width from a local line center such as appears to be the case for the $2\nu[\text{R}(12)]$ and the $2\nu[\text{R}(14)]$ lines. However, the self broadening term of Equation (42) becomes negative for frequencies within one line width of a local line center. This leads to a general second order polynomial of the form,

$$k(\nu) = A p_a - B p_a^2 [\text{km}^{-1}] , \quad (47)$$

where

$$A = \frac{p_T C_N}{RT} [\text{km}^{-1} \text{ torr}^{-1}]$$

$$B = \frac{C_S + C_N}{RT} [\text{km}^{-1} \text{ torr}^{-2}] .$$

The $2\nu[R(18)]$ line should follow the form shown in Equation (47) since it is within the line width of a local absorption line.

Thus, the absorption coefficient as a function of water vapor pressure for a frequency within a line width of line center will have linear or parabolic down characteristics (negative second order coefficient); whereas the absorption function for frequencies outside of a line width will display a linear or parabolic up characteristic with the curve becoming more parabolic as C_S becomes much larger than C_N . Equation (42) can be expressed yet another way,

$$k(\nu) = \frac{C_N}{RT} p_a (p_N + B p_a) \text{ [km}^{-1}\text{]} \quad (48)$$

where

$$B = \frac{C_S}{C_N} .$$

B is large in the window regions where absorption is due to the wings of far away lines. In the $10 \mu\text{m}$ region, for example, B ranges from 200 to 300. The quadratic term, therefore, dominates in this region and the absorption coefficient versus water vapor partial pressure is parabolic.

In the high absorption region of this study, where the absorption is due primarily to local lines, B is small (5 - 10) and thus the absorption coefficient versus water vapor partial pressure functions are nearly linear.

3. A Least Squared Curve Fit to the Data and Analysis

Using the general second order polynomial form of the absorption coefficient given in Equation (46), a least squared curve fit was made for the experimental data displayed in Figures 4.2 through 4.10. The resulting equations are presented in Table 4.5 along with the least squared fit equations determined from the TN model theoretical values given in Figures 4.2 through 4.10.

The absorption coefficient functions of this heavy local line absorption region appear nearly linear as predicted by the TN model and observed by past studies of heavy absorption regions. The theoretical second order term is two orders of magnitude smaller than the linear term for the $2\nu[R(12)] = 1941.096 \text{ cm}^{-1}$ line and the $2\nu[R(14)] = 1943.862 \text{ cm}^{-1}$ line, and four orders of magnitude smaller for the $2\nu[R(18)]$ line which is much closer to line center. The data appears to agree with the theoretical functions in at least the linear term for the $2\nu[R(12)]$ and the $2\nu[R(18)]$ lines at 295°K and 310°K. The agreement in the linear term with the model for the $2\nu[R(14)]$ data seems to be less close than for the other two lines. All of the linear terms for the data at 295°K and 310°K are consistently higher than the TN model predicts. Since there is such a small amount of accurate data to go on, it is difficult to say where the inaccuracy lies -in the data or in the model.

As for the quadratic terms of the experimental measurements, they seem to differ in sign from their theoretical counterparts for all except the $2\nu[R(12)]$ line at 310°K. The difference between the

TABLE 4.5

EXPERIMENTAL AND THEORETICAL ABSORPTION COEFFICIENT

$k(\text{km}^{-1}) = A_p + B_p^2$ WITH WATER PRESSURE p IN TORR FOR
THE INVESTIGATED LASER LINES

WAVENUMBER (cm^{-1})	TEMPERATURE ($^{\circ}\text{K}$)	EXPERIMENTAL ABSORPTION COEFFICIENT EQUATION	THEORETICAL ABSORPTION COEFFICIENT EQUATION
1941.096	295	$(1.05)p - (1.95\text{E}-3)p^2$	$(9.00\text{E}-1)p + (6.68\text{E}-3)p^2$
1941.096	310	$(1.09)p + (3.24\text{E}-3)p^2$	$(9.92\text{E}-1)p + (5.63\text{E}-3)p^2$
1941.096	323	$(8.53\text{E}-1)p + (0.0)p^2$	$(9.33\text{E}-1)p + (6.91\text{E}-3)p^2$
1943.862	295	$(1.19)p - (6.68\text{E}-3)p^2$	$(9.14\text{E}-1)p + (6.72\text{E}-3)p^2$
1943.862	310	$(1.19)p - (3.63\text{E}-3)p^2$	$(8.94\text{E}-1)p + (6.45\text{E}-3)p^2$
1943.862	323	$(1.09)p - (3.30\text{E}-3)p^2$	$(8.75\text{E}-1)p + (6.21\text{E}-3)p^2$
1949.245	295	$(1.42)p - (1.62\text{E}-2)p^2$	$(1.20)p + (7.06\text{E}-4)p^2$
1949.245	310	$(1.72)p - (9.95\text{E}-3)p^2$	$(1.51)p + (4.61\text{E}-4)p^2$
1949.245	323	$(1.68)p + (0.0)p^2$	$(1.80)p + (5.97\text{E}-4)p^2$

experimental and theoretical quadratic terms may be within the experimental error of the measurements. The instability of the background measurement has made the absorption measurements too imprecise to determine this small quadratic term with confidence.

The data measured at 323°K illustrates the difficulties encountered toward the end of the experiment. The background measurements became less stable. As a result, not enough data was gathered to even estimate a quadratic term for the $2\nu[R(12)]$ and $2\nu[R(18)]$ lines. As Figure 4.8 indicates, the most data gathered for this temperature was for the $2\nu[R(14)]$ line and indeed Table 4.5 shows this data pretty much falling into the same range of agreement as data at the lower temperatures. In fact, the data for this $2\nu[R(14)]$ line at 323°K with respect to its linear term, seems to agree with the theoretical linear term even better than $2\nu[R(14)]$ data measured at the lower temperatures.

Although the data has a wide margin of uncertainty, the overall indications seem to be that it is substantiating the TN model line shape. However, it is clear that much more sensitive data must be taken before any definite improvements can be made in the model resulting from observations of the local line shapes as a function of temperature for this region. Until such time as more accurate data is obtained, it is pointless to analyze this data any further.

CHAPTER V

CONCLUSIONS

Water vapor absorption in the window regions of the near infrared is of considerable interest to many infrared energy transmission systems. A controversy exists as to what the cause or causes are for the water vapor continuum absorption observed in these window regions. One school of thought says that it is a result of complex clusters of water molecules (i.e, dimers) that absorb radiation as a slow varying function of frequency throughout the entire near infrared region. Important to the support of this dimer theory is the fact that it explains the negative temperature dependence of the continuum.

Another school of thought says that the continuum is from the far wing overlap into these window regions of very strong absorption lines centered deep in the vibrational bands of H_2O . A line shape model which is Lorentzian out to 5 cm^{-1} from line center and modified in the far wings was developed at Ohio State University in 1976-79 by Michael E. Thomas and Dr. Robert J. Nordstrom. The form of the far wing shape was developed theoretically and then certain line shape parameters were derived by trial and error fit to data taken in regions of high

absorption dominated by local absorption lines. Thus, the model was developed in regions where the continuum is of little significance and therefore, the development was independent of any continuum effects. It was then applied to the window regions and was the first line shape model to successfully model the pressure and temperature characteristics of the continuum. Although the model fell short of modeling the magnitude of the negative temperature dependence, it did show a negative dependence in temperature for the continuum absorption.

The purpose of this study was to gather temperature dependence data in a region dominated by local line absorption so that the line shape parameters used in the Thomas-Nordstrom model can be improved on and more insight can be made as to the temperature dependence of these line shapes. The study uses a frequency doubled CO₂ laser frequency probe to examine the 5.15 μm infrared region at three frequency doubled lines:

- 1) $2\nu[R(12)] = 1941.0952 \text{ cm}^{-1}$
- 2) $2\nu[R(14)] = 1943.8624 \text{ cm}^{-1}$
- 3) $2\nu[R(18)] = 1949.2495 \text{ cm}^{-1}$.

These lines were examined at temperatures of 295°K, 310°K, and 323°K with the sample pressures set to 5, 10, and 15 torr. All of the samples were nitrogen broadened to 740 torr.

Unfortunately, no solid conclusions or new insights can be made from the data gathered during this study due to the experimental instabilities of the optical and detection systems and therefore, the inaccuracy of the measurements. It would appear that the data supports

the gross features of the models' ability to predict the absorption coefficient versus water vapor partial pressure for the temperatures investigated. It is clear, however, that much more accurate data must be measured for these lines before any real improvements in the model can be made. The instability of the system and thus the inability to maintain a constant background throughout the measurements was the major problem encountered in this first attempt to obtain this data.

These instabilities were identified in two areas. First it was discovered that the signal detector was giving fluctuating readings seemingly dependent on how much nitrogen remained in its dewar. These fluctuations were independent of the CO₂ laser and the second harmonic generation because the laser source during these observations was a Helium Neon laser. When the signal detector was replaced by a HgCdTe detector, which was the only other detector available, a stable background was measured. It is highly recommended that the signal detector be replaced with a new InSb detector.

The other instability identified was in the CO₂ laser. Using the HgCdTe detector as the signal detector, only the CO₂ laser was reintroduced into the system and the background measurements were again unstable. It was never determined how this laser could produce fluctuations in the background, but it is recommended that the Sylvania CO₂ laser previously described [26] be used as the radiation source. The Sylvania laser has a cw power output of 2 to 3 watts which has been

found to be sufficient to produce a measurable amount of second harmonics. At the beginning of the project, it was believed that 10 watts cw would be required in order to produce a reasonable amount of second harmonics and thus the reason for constructing the new laser. As it turned out, in order to be assured of a TEM₀₀ mode for the output of the new laser, an iris was required in the cavity which decreased the laser's power to the same range as the Sylvania laser. The Sylvania is the better of the two lasers for this output power range and should therefore be brought back into working order and put into the optical system.

The exact role in the instability problem of the CdGeAs₂ crystal and nitrogen dewar was never determined. It was found that the dewar had to be suspended in order to keep the outer skin thermal expansion and contractions of the dewar from disorienting the crystal. This problem was encountered when the dewar was resting on a pedestal and supported by its tail piece.

The crystal's face has been pitted by exposure to radiation of too much intensity and there only seems to be one spot on the crystal face where a fair amount of second harmonic energy is observed when exposed to the CO₂ radiation. Therefore, getting a new crystal would be the best direction to take in constructing a better system. Now that the crystal focusing optics have been developed there would be no need to expose a new crystal to high input power intensities and so crystals used in the future should be safe from face surface damage.

Once these improvements in the system are made, data should be retaken for the three laser lines investigated in this study at similar, if not the same, temperatures. If this data appears to be accurate enough, the C_S self-broadening coefficients should be determined from the data and their characteristics as a function of temperature observed. In addition, the $2\nu[R(20)]$ line should be investigated as a possible partner in an on-line/off-line resonance differential absorption LIDAR pair with the $2\nu[R(18)]$ line. The $2\nu[R(18)]$ laser line is well within the halfwidth of a fairly strong local absorption line and the $2\nu[R(20)]$ line sits within a narrow window of this $5.15\ \mu\text{m}$ region.

REFERENCES

- [1] McCoy, J.H., Rensch, D.B. and Long, R.K., Appl. Opt. 8, 1471 (1969).
- [2] Burch, D.E., Aeronutronic Publication No. U-4784, Semi-Annual Technical Report, AFCRL Contract No. F19628-69-C-0263, U.S. Air Force (1970).
- [3] Arefev, V.N., Dianov-Klokov, V.I. Radionov, V.F. and Sizov, N.I., Opt. and Spectroc. 39, 560 (1975) (Opt. i Spektrosk, 39, 982 1975)).
- [4] Nordstrom, R.J., Thomas, M.E., Peterson, J.C., Damon, E.K. and Long, R.K., Appl. Opt. 17, 2724 (1978).
- [5] Peterson, J.C., Thomas, M.E., Nordstrom, R.J., Damon, E.K. and Long, R.K., Appl. Opt. 18, 834 (1979).
- [6] White, K.O., Watkins, W.R., Bruce, C.W., Meridth, R.E. and Smith, F.F., Appl. Opt. 17, 2711 (1978).
- [7] Meridth, R.E., Tuer, T.W. and Woods, D.R., Investigation of DF Laser Propagation, SAI Tech. Report (1974).
- [8] Elsasser, W.M., "Heat Transfer by Infrared Radiation in the Atmosphere", Harvard University Press, Cambridge, Mass. (1942).
- [9] Shaw, J.H., Ohio Journal of Science 53, 253 (1953).
- [10] Montgomery, G.P., Jr., Appl. Opt. 17, 2299 (1978).
- [11] Varanasi, P.S., Chou, S. and Penner, S.S., J. Quant. Spectros. Radiat. Transfer. 8, 1537 (1968).
- [12] Penner, S.S., J. Quant. Spectrosc. Radiat. Transfer. 13, 383 (1973).
- [13] Carlson, H.R., Appl. Opt., 10, 2297 (1971).

- [14] Carlon, H.R., "Final Report: Infrared Absorption by Water Clusters", Chemical Systems Laboratory, Report No. ARCSL-TR-79013, March 1979.
- [15] Thomas, M.E., Technical Report 784701-5, Contract DAAG-29-77-C-0010, U.S. Army Research Office (1979).
- [16] McClatchey, R.A., Benedict, W.S., Clough, S.A., Burch, D.E., Calfee, R.F., Fox, K., Rothman, L.S. and Garing, J.S., U.S. Air Force Research Laboratories, AFCRL-TR-73-0096, Bedford, Massachusetts (1973).
- [17] Burch, D.E., Gryvnak, D.A. and Gates, F.J., AFCRL-TR-74-0377, U.S. Air Force (1974).
- [18] Watkins, W.R., Spellicy, R.L., White, K.D., Sojka, B.Z. and Bower, L.R., Appl Opt. 18, 1582 (1979).
- [19] Long, R.K., Mills, F.S. and Trusty, G.L., Contract Number F30602-72-C-0016, Advanced Research Projects Agency (1973).
- [20] Deutchman, E.M. and Calfee, R.F., "Two Computer Programs to Produce Theoretical Absorption Spectra of Water Vapor and Carbon Dioxide", AD816 369, April 1967.
- [21] Varanasi, P. and Ko, F.K., "Intensity Measurements in the 2 μ m CO₂ Bands at Low Temperatures", presented at 33rd Symposium on Molecular Spectroscopy, The Ohio State University, 1978.
- [22] Fomin, V.V. and Tvorogov, S.D., Appl. Opt., 12, 584, (1973).
- [23] Menyuk, N., Iseler, G.W. and Mooradian, A., Applied Phys. Letters 29, 422 (1976).
- [24] Zernike, F. Midwinter, J.E., Applied Nonlinear Optics, Wiley Press, 1973.
- [25] Long, R.K., Damon, E.K., Peterson, J.C. and Thomas, M.E., "Laser Atmospheric Absorption Studies", Rome Air Development Center, Report No. RADC-TR-76-330, June 1978.
- [26] Long, R.K., "Absorption of Laser Radiation in the Atmosphere", The Ohio State University ElectroScience Laboratory, Report 1579-3, May 1963: prepared under Contract AF33(657)-10824 for Air Force Avionics Laboratory (AD 410571).

- [27] Peterson, J.C., "A Study of Water Vapor Absorption at CO₂ Laser Frequencies Using a Differential Spectrophone and White Cell", Dissertation, The Ohio State University, June 1978.
- [28] White, J.U., J. Opt. Soc. Amer. 32, 285, (1942).

**DATA
FILM**